Unshielded Precipitation Gauge Collection Efficiency with Wind Speed and Hydrometeor Fall Velocity~~. Part II: Experimental Results~~

Jeffery Hoover[1], Michael E. Earle[1], Paul I Joe[1], Pierre E. Sullivan[2]

[1]Environment and Climate Change Canada, Toronto, ON, M3H 5T4, Canada
[2]Department of Mechanical and Industrial Engineering, University of Toronto, Toronto, ON, M5S 3G8, Canada

Correspondence to: Jeffery Hoover (jeffery.hoover@canada.ca)

Abstract. ~~Five~~ ~~C~~collection efficiency transfer functions that compensate for wind-induced collection loss are presented and evaluated for unshielded precipitation gauges~~ are presented that compensate for wind-induced collection loss~~. Three ~~of the~~novel transfer functions ~~presented are dependent on~~with wind speed and precipitation fall velocity dependence~~, and were~~were derived ~~through~~ using computational fluid dynamics modelling ~~in Part 1~~ (CFD function) and ~~from~~ measurement data (HE1 function with fall velocity threshold and HE2 function with linear fall velocity dependence). These functions are evaluated alongside universal ($K_{Universal}$) and ~~site~~climate-specific (K_{CARE}) transfer functions with wind speed and temperature dependence. ~~Their~~ Transfer function performance ~~was~~ is assessed using 30-minute precipitation event accumulations reported by unshielded and shielded Geonor T-200B3 precipitation gauges over two winter seasons. The latter gauge was installed in a Double Fence Automated Reference (DFAR) configuration~~ comprising a single Alter shield within an octagonal, wooden double fence~~. Estimates of fall velocity were provided by a Precipitation Occurrence Sensor System (POSS).

The CFD function reduced the RMSE (0.08 mm) relative to $K_{Universal}$ (0.20 mm), K_{CARE} (0.13 mm), and the unadjusted measurements (0.24 mm), with a bias error of 0.011 mm. The HE1 function provided a RMSE of 0.09 mm and bias error of 0.006 mm, capturing well the collection efficiency trends for rain and snow. The HE2 function better captured the overall collection efficiency, including mixed precipitation, resulting in a RMSE of 0.07 mm and bias error of 0.006 mm. ~~The improved agreement demonstrates~~ These functions are assessed across solid and liquid hydrometeor types and for temperatures between -22 °C and 19 °C. The results demonstrate that transfer functions incorporating hydrometeor fall velocity can dramatically reduce the uncertainty of adjusted precipitation measurements relative to functions based on temperature.~~ the importance of fall velocity for collection efficiency~~.

Commented [JH1]: Part I: modelling results added to Part II: experimental results manuscript.

1 Introduction

~~This work develops and assesses transfer functions incorporating hydrometeor fall velocity to reduce the uncertainty (RMSE) in collection efficiency and precipitation accumulation estimates from unshielded Geonor T-200B3 precipitation gauges.~~

Automated catchment-type precipitation gauge measurements are critical as references for, and input to, weather, climate, hydrology, transportation, and remote sensing applications. The systematic bias and uncertainty of ~~these~~ gauge~~s~~ measurements due to wind-induced undercatch is a major challenge, particularly with respect to the measurement of mixed and solid precipitation (Rasmussen et al., 2012;Kochendorfer et al., 2018). For example, an unshielded weighing precipitation gauge can capture less than 50% of the actual amount of solid precipitation falling in air when the wind speed exceeds 5 m s^{-1} (Kochendorfer et al., 2017b). This measurement challenge has prompted: (1) modelling studies to better understand and visualize the undercatch of hydrometeors by precipitation gauges; and (2) the development of transfer functions to adjust measurements for undercatch effects. Previous work in each of these domains is outlined in Sections 1.1 and 1.2, respectively. The objectives of the present study, which implements numerical modelling and experimental analysis to develop transfer functions with wind speed and hydrometeor fall velocity dependence, are presented in Section 1.3.

1.1 Modelling studies

Computational fluid dynamics (CFD) studies have been used to simulate the airflow around precipitation gauges and the associated collection efficiencies for rain and solid precipitation (Nešpor and Sevruk, 1999;Constantinescu et al., 2007;Colli, 2014;Colli et al., 2014;Colli et al., 2015;Colli et al., 2016a;Colli et al., 2016b;Thériault et al., 2012;Thériault et al., 2015;Baghapour and Sullivan, 2017;Baghapour et al., 2017). These studies have demonstrated the influence of wind speed, turbulence, hydrometeor characteristics (size, density, drag, terminal velocity), and gauge and shield geometry on precipitation gauge undercatch. For rainfall, Nešpor and Sevruk (1999) showed increases in wind-induced error for smaller drop sizes with lower terminal velocities, with errors increasing for higher wind speeds. The conversion factor (inverse of integral collection efficiency) varied with the precipitation intensity and rainfall type, which influenced the distribution of hydrometeor sizes and terminal velocities. Thériault et al. (2012) demonstrated similar trends for snowfall, with collection efficiencies varying significantly with the type of solid precipitation and size distribution. Simulated collection efficiencies for wet snow and dry snow hydrometeors captured the general upper and lower bounds of experimental observations, respectively, with the lower collection efficiency for dry snow hydrometeors attributed to their lower terminal velocity and interaction with the local airflow around the gauge.

For a Geonor gauge with single-Alter shield, Thériault et al. (2012) used a constant drag coefficient hydrometeor tracking model to develop a series of ~~adjustments~~transfer functions based on wind speed for different hydrometeor types. Colli et al. (2015) extended this work to show the influence of different hydrometeor drag models on collection efficiency results. Empirical drag model results (Khvorostyanov and Curry, 2005), based on the relative hydrometeor-to-air velocity over the hydrometeor trajectory, were shown to yield higher collection efficiencies compared with constant drag coefficient results that

can overestimate drag values. Colli et al. (2015) developed ~~adjustments~~transfer functions based on wind speed for unshielded and single-Alter-shielded gauges for three specific hydrometeor size distributions. Further studies, using computationally intensive Large Eddy Simulation models, better resolved the intensity and spatial extent of turbulence around the gauge orifice, which can lead to temporal variations in collection efficiency results (Colli et al., 2016a;Colli et al., 2016b;Baghapour and Sullivan, 2017;Baghapour et al., 2017). The degree of turbulence was found to vary depending on the specific shield configuration and wind speed (Baghapour et al., 2017).

~~The computational fluid dynamics analysis presented in Hoover et al. (2020, hereafter Part I) characterized the collection efficiency dependence on wind speed and precipitation fall velocity for different precipitation types. Collection efficiencies were shown to be similar for different hydrometeor types with identical fall velocities, enabling the development of a universal transfer function based on wind speed and hydrometeor fall velocity. The use of precipitation fall velocity offers a physically-based approach to improve adjustment functions by exploiting the aerodynamic properties of falling precipitation that influence collection efficiency. This information may be provided by instruments such as present weather sensors and disdrometers.~~

1.2 Transfer functions

Intercomparisons of precipitation gauges have served as the primary mechanism for developing transfer functions. ~~Intercomparisons to assess gauge undercatch have demonstrated that an unshielded weighing precipitation gauge can capture less than 50% of the actual amount of solid precipitation falling in air when the wind speed exceeds 5 m s^{-1} (Kochendorfer et al., 2017b). Various adjustment functions have been proposed to compensate for undercatch, based on measured wind speed and air temperature (Goodison, 1978;Yang et al., 1998;2005;Yang and Simonenko, 2013;Yang, 2014;Rasmussen et al., 2001;Smith, 2007;Wolff et al., 2015;Kochendorfer et al., 2017a).~~

In the 1998 World Meteorological Organization (WMO) Solid Precipitation Measurement Intercomparison, ~~adjustments~~ transfer functions were determined experimentally~~, primarily for manual gauges,~~ by ~~comparison~~ comparing measurements from different gauges (primarily manual) with those from a~~to~~ manual ~~reference measurements of precipitation using a~~ collector with a Tretyakov shield in the WMO Double Fence Intercomparison Reference (DFIR) configuration (Goodison et al., 1998). Precipitation events were monitored by observers, who reported the amount and type of snow, wind speed, and temperature statistics for each event. Events were defined based on the duration of continuous snowfall when the reference DFIR precipitation accumulation was greater than or equal to 3 mm. A~~a~~djustment functions for unshielded gauge collection efficiencies were recommended for snow, mixed precipitation, and rain, based on the wind speed at gauge height (Goodison, 1978;Goodison et al., 1998;Yang et al., 1998). While these adjustments could be applied to ~~provided improvements for~~ manual precipitation accumulation measurements, their application to automated measurements at shorter time scales, and where the precipitation type may not be well defined, presents a significant challenge (Colli, 2014;Colli et al., 2014;Colli et al., 2016a;Colli et al., 2016b;Thériault et al., 2015;Thériault et al., 2012)

The WMO commissioned another intercomparison, the Solid Precipitation Intercomparison Experiment (SPICE), to assess various automated technologies for the measurement of precipitation accumulation and snow depth, and to recommend automated field reference systems (Nitu et al., 2018). An automated precipitation gauge configured with a single-Alter shield within a DFIR fence was chosen as the field reference configuration for precipitation accumulation; this was referred to as the Double Fence Automated Reference (DFAR) configuration. ~~For assessment purposes, precipitation events were defined as 30-minute periods with ≥ 0.25 mm precipitation captured by the reference gauge and ≥ 60% (18 minutes) precipitation occurrence as indicated by a disdrometer. This approach was selected to ensure confidence in reference measurement accumulations relative to gauge uncertainties (e.g. due to wind and temperature), with sufficiently short duration to capture the event conditions (e.g. wind, temperature, precipitation characteristics) within dynamic environments (Kochendorfer et al., 2017a).~~

Transfer functions for unshielded and shielded gauges were derived as an exponential function of wind speed following the approach of Goodison (1978) and using 30-minute precipitation events from the SPICE data set (Kochendorfer et al., 2017a). Separate functions were developed for solid precipitation and mixed precipitation, as defined by air temperature ranges: less than -2 °C for solid precipitation, and between -2 °C and 2 °C for mixed precipitation. ~~These functions were based on an exponential model for collection efficiency as a function of wind speed only (Goodison, 1978).~~

Using Bayesian analysis of Norwegian measurement data, Wolff et al. (2015) developed a precipitation phase-independent, continuous transfer function with respect to wind speed and air temperature for a single-Alter shielded Geonor precipitation gauge. A similar, but less complex, function was developed by Kochendorfer et al. (2017a;2018) using the SPICE data set, including results from eight measurement sites in Canada, Norway, Finland, Switzerland, and the USA. The application of this "universal" function to precipitation accumulation measurements from unshielded weighing gauges in SPICE was shown to reduce the overall bias relative to the DFAR; however, reductions in the root mean square error (RMSE) ~~was~~ were less significant (Kochendorfer et al., 2017a;2017b;2018;Wolff et al., 2015). ~~The RMSE values for adjusted measurements were on the order of 0.20 mm (Kochendorfer et al., 2017a); however, a separate comparison of replicate configurations of weighing gauges with single-Alter, double-Alter, and US small DFIR shields at the US WMO-SPICE site exhibited errors of 0.09 mm, 0.08 mm, and 0.07 mm, respectively (Kochendorfer et al., 2017b), indicating that further reductions in RMSE are possible.~~

When applying ~~The errors, based on~~ universal adjustments with wind speed and air temperature dependence, the errors can vary significantly by site, presumably driven by differences in climatology (Smith et al., 2020;Kochendorfer et al., 2017a). This has motivated further work on ~~site- and~~ climate-specific transfer functions (Koltzow et al., 2020;Smith et al., 2020). Other studies have proposed the use of precipitation intensity for the improved adjustment of solid precipitation (Chubb et al., 2015;Colli et al., 2020). Another potential avenue for reducing errors in adjusted measurements is by improving the ability of transfer functions to distinguish among different precipitation types and their aerodynamic properties (Thériault et al., 2012;Wolff et al., 2015;Nešpor and Sevruk, 1999).

1.3 Objectives

Computational fluid dynamics (CFD) studies simulate the airflow around precipitation gauges and the associated collection efficiencies for rain and solid precipitation (Nešpor and Sevruk, 1999;Constantinescu et al., 2007;Colli, 2014;Colli et al., 2014;Colli et al., 2015;Colli et al., 2016a;Colli et al., 2016b;Thériault et al., 2012;Thériault et al., 2015;Baghapour and Sullivan, 2017;Baghapour et al., 2017). These studies have demonstrated the influence of wind speed, turbulence, hydrometeor characteristics (size, density, drag, terminal velocity), and gauge and shield geometry on precipitation gauge undercatch. For rainfall, Nešpor and Sevruk (1999) showed increases in wind-induced error for smaller drop sizes with lower terminal velocities, with errors increasing for higher wind speeds. The conversion factor (inverse of overall integral collection efficiency) varied with the precipitation intensity and rainfall type, which influenced the distribution of hydrometeor sizes and terminal velocities. Thériault et al. (2012) demonstrated similar trends for snowfall, with collection efficiencies varying significantly with hydrometeor typetype of solid precipitation and size distribution. Simulated collection efficiencies for wet snow and dry snow hydrometeors captured the general upper and lower bounds of experimental observations, respectively, with the lower collection efficiency for dry snow hydrometeors attributed to their lower terminal velocity and interaction with the local airflow around the gauge.

For a Geonor gauge with single-Alter shield, Thériault et al. (2012) used a constant drag coefficient hydrometeor tracking model to develop a series of adjustments based on wind speed for different hydrometeor types. Colli et al. (2015) extended this work to show the influence of different hydrometeor drag models on collection efficiency results. Empirical drag model results (Khvorostyanov and Curry, 2005), based on the relative hydrometeor-to-air velocity over the hydrometeor trajectory, were shown to yield higher collection efficiencies compared with constant drag coefficient results that can overestimate drag values. Colli et al. (2015) developed adjustments based on wind speed for unshielded and single-Alter-shielded gauges for three specific hydrometeor size distributions. Further studies, using computationally intensive Large Eddy Simulation models, have better resolved the intensity and spatial extent of turbulence around the gauge orifice, which can lead to temporal variations in collection efficiency results (Colli et al., 2016a;Colli et al., 2016b;Baghapour and Sullivan, 2017;Baghapour et al., 2017). The degree of turbulence varies depending on the shielding and wind speed (Baghapour et al., 2017).

Collection efficiency results have been shown to be highly dependent on the hydrometeor fall velocity (Nešpor and Sevruk, 1999;Thériault et al., 2012;Colli et al., 2016b;Hoover et al., 2020). The computational fluid dynamics analysis presented in Hoover et al. (2020, hereafter Part I) characterized the collection efficiency dependence on wind speed and precipitation fall velocity for different precipitation types. Collection efficiencies were shown to be similar for different hydrometeor types with identical fall velocities, enabling the development of a universal transfer function based on wind speed and hydrometeor fall velocity. The use of precipitation fall velocity offers a physically-based approach to improve adjustment functions by exploiting the aerodynamic properties of falling precipitation that influence collection efficiency. This information may be provided by instruments such as present weather sensors and disdrometers.

In this work, adjustment functions incorporating hydrometeor fall velocity are developed to reduce the uncertainty (RMSE) in collection efficiency and precipitation accumulation estimates from unshielded Geonor T-200B3 precipitation gauges. ~~In this work, adjustment functions are developed and evaluated for unshielded Geonor T-200B3 weighing precipitation gauges.~~ The unshielded gauge configuration allows for the assessment of a broader range of collection efficiencies, as the degree of undercatch is generally more pronounced for unshielded gauges relative to shielded configurations. Further, by focussing on the unshielded configuration, no assumptions are required regarding the behaviour of the shield slats and their role in momentum reduction and turbulence generation around the gauge.

A combined modelling and experimental approach is used in this study. In the modelling component, computational fluid dynamics and Lagrangian analysis is used to characterize the gauge collection efficiency dependence explicitly in terms of wind speed and hydrometeor fall velocity, and to derive a corresponding transfer function. In the experimental component, fall velocity and precipitation type estimates from a Precipitation Occurrence Sensor System (POSS) are used to investigate how the hydrometeor properties influence the relationships among measured catch efficiency, wind speed, and temperature. Two additional transfer functions are derived experimentally with wind speed and fall velocity dependence. ~~For this study, three transfer functions with wind speed and fall velocity dependence are~~ developed and ~~assessed, including the~~ a ~~CFD transfer function developed in Part I~~through ~~numerical modelling and two other transfer functions (HE1 and HE2) developed experimentally herein. The Precipitation Occurrence Sensor System (POSS) was used to estimate fall velocities and hydrometeor types for the assessment.~~ These new transfer functions are assessed against transfer functions with dependence on wind speed and air temperature, including one of the universal functions developed by Kochendorfer et al. (2017a) and a ~~site~~climate-specific function ~~determined~~ derived herein using a similar methodology.

2 Modelling method

Commented [JH2]: Sect. 2 added from Part I

2.1 Computational fluid dynamics model

A high-resolution 3-dimensional computer aided design model of the Geonor T-200B3 600 mm capacity gauge (hereafter Geonor gauge) with 2 m gauge orifice height was developed for the analysis using SolidWorks engineering software (Fig~~s~~. 1~~a and b~~). The Geonor gauge was modelled with a 200 cm^2 orifice, 3.15 mm orifice thickness, and full 360 mm length inlet extending down into the gauge housing. SolidWorks Flow Simulation software (SolidWorks, 2019) was used to simulate the time-averaged 3-dimensional flow around the unshielded precipitation gauge. Favre-averaged Navier-Stokes equations were used to relate the fluid density, velocity components, viscous shear stress, Reynolds (turbulence) stress tensor, and mass distributed external force per unit mass, with contributions from porous media resistance, gravitational acceleration, and the coordinate systems rotation. The fluid was modelled as isothermal and incompressible. Bulk turbulence through the fluid was captured using the k–ε turbulence model with 5 % turbulence intensity at the inlet (Kato and Launder, 1993). A modified wall

functions approach using Van Driest's profile was used to characterize the flow in the near-wall region (SolidWorks, 2013, 2019).

The domain width was 7 m and height was 8 m to achieve undisturbed flow at the edges of the domain and ensure uniform flow near the modeled gauge. The length of the domain was 18 m to allow hydrometeors to be released from a horizontal plane in the free-stream airflow ahead of the gauge (Fig. 1~~a~~, Table 1). The ground was modelled as an adiabatic frictionless wall, with horizontal wind speeds ~~u~~U_w applied in 1 m s^{-1} increments from 0 to 10 m s^{-1}. A finite-volume approach with rectangular parallelepipeds for fluid cells and polyhedrons at fluid solid interfaces was used for mesh generation. ~~Control planes were centered around the gauge axis for mesh symmetry around the gauge, with the x-axis along the length of the domain in the wind direction, y-axis crosswise across the domain width, and the z-axis in the vertical direction.~~ A clustered mesh with first-order refinement around the gauge (8 mm cells) and secondary refinement of 2 mm cells around the mounting post, gauge, and orifice (8.3 million cells in total) was used to resolve the nonlinear updraft velocity profile around the leading edge of the gauge rim and fluid dynamics in the area of the orifice ~~(Figs. 1c and d).~~ ~~The same mesh was utilized at each of the wind speeds used in the analysis, with maximum y^+ values verified to be less than 100 at all wind speeds (Launder and Spalding, 1974;Spalding, 1961).~~ Simulations for each of the wind speeds were run to convergence for mass, energy, and momentum with model details summarized in Table 1.

Table 1. Computational fluid dynamics and Lagrangian hydrometeor tracking model

Component	Description
Model	Favre-averaged Navier-Stokes, steady-state, *k-ε*, isothermal, incompressible, gravitational acceleration a_z = -9.81 m s^{-2}
Fluid	Air (gas): molecular mass 0.02896 kg mol^{-1}
Boundary conditions	Ground: ideal wall (adiabatic, frictionless)
Initial and ambient conditions	P = 101325 Pa, T = 293.2 K, ~~u~~U_w = 0,1,2,…,10 m s^{-1} (free-stream wind speed along x)
Domain	Length x = 18 m, width y = 7 m, height z = 8 m
Mesh	8.3 million cells, y^+_{mean} = 2.5 y^+_{max} =15.1 (~~u~~U_w=1 m s^{-1}), y^+_{mean} =17.2 y^+_{max} =90.8 (~~u~~U_w=10 m s^{-1})
Hydrometeor injection	Horizontal injection rectangle: length x = 5.5 m, width y = 0.4 m, height z = 2 to 8 m 100000 hydrometeors/rectangle (~4.5 hydrometeors/cm^2)
Hydrometeor tracking	Lagrangian, uncoupled, spherical hydrometeors, elastic wall reflection inside gauge orifice

Formatted: Font: Not Italic

Formatted: Font: Not Italic

Formatted: Font: Not Italic

Formatted: Font: Not Italic

Formatted: Font: Not Italic

Formatted: Font: Not Italic

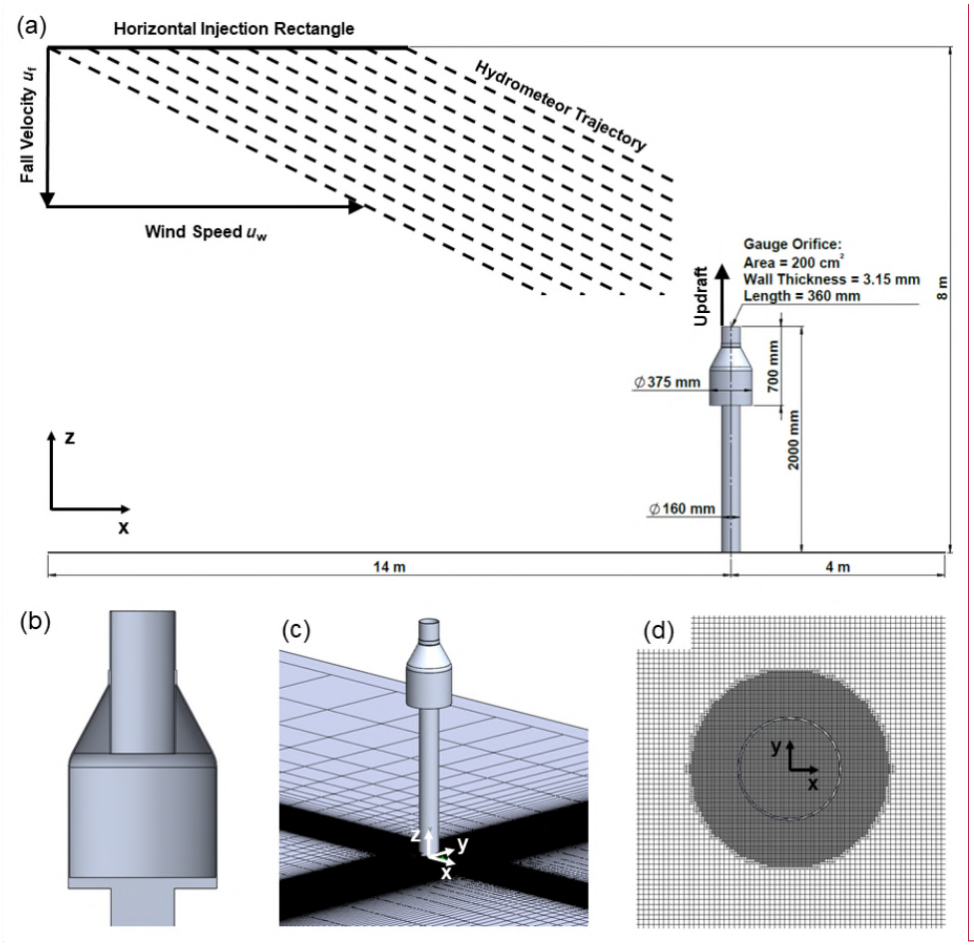

Commented [JH3]: Replaced

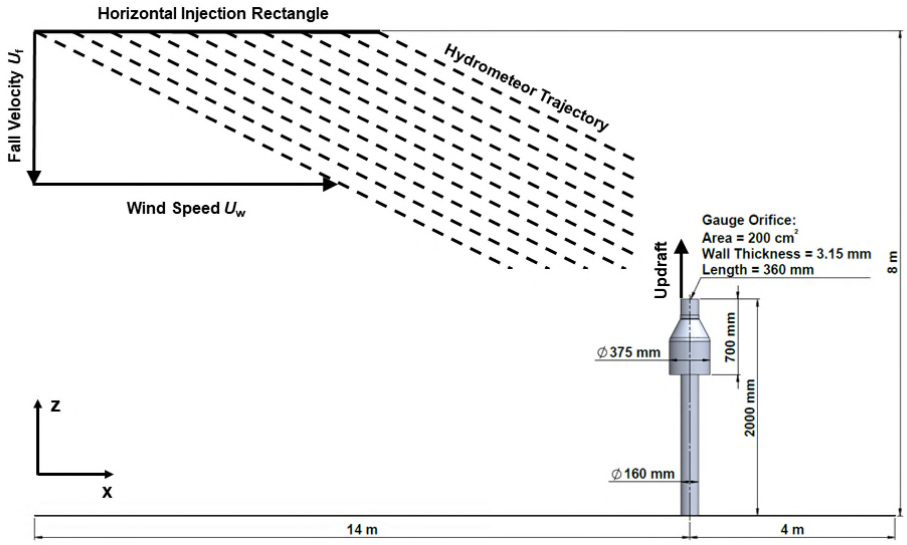

Figure 1. Unshielded Geonor T-200B3 600mm capacity gauge and model geometry, including computational domain with ground, horizontal hydrometeor injection rectangle, free-stream hydrometeor trajectories based on wind speed and hydrometeor fall velocity and local updraft around leading edge of gauge orifice.

2.2 Collection efficiency based on hydrometeor fall velocity and wind speed

For each wind speed, monodispersed hydrometeors were injected from a horizontal plane upstream and above the gauge orifice (Fig. 1a). Hydrometeor types were characterized by their fall velocity, diameter, density, and mass (Table 2). For dry snow and wet snow, the hydrometeor sizes are related to the fall velocity by a general power law (Rasmussen et al., 1999). The fall velocity for dry snow U_{dry} (cm s^{-1}) is a function of the size D_{dry} (cm), with a similar relationship for wet snow (Eqs. 1a and b).

$$U_{dry} = 107 D_{dry}^{0.2}, \quad (1a)$$

$$U_{wet} = 214 D_{wet}^{0.2}, \quad (1b)$$

For dry snow and wet snow, the hydrometeor density was chosen such that the size and fall velocity followed the power law relationship of Rasmussen et al. (1999), with the drag coefficient for spherical hydrometeors given by Henderson (1976) based

Field Code Changed
Field Code Changed
Field Code Changed
Field Code Changed

on the relative hydrometeor to air velocity. This drag formulation closely matches that of Haider and Levenspiel (1989), and has been used in previous studies (Baghapour and Sullivan, 2017).

Table 2. Characteristics for rain, dry snowflake, wet snowflake, and ice pellet hydrometeors.

Description	Diameter (m)	Density (kg m^{-3})	Mass (kg)	Fall Velocity (m s^{-1})
Rain	9.989E-05	9.982E+02	5.209E-10	0.25
Rain	1.571E-04	9.982E+02	2.028E-09	0.50
Rain	2.121E-04	9.982E+02	4.986E-09	0.75
Rain	2.671E-04	9.982E+02	9.956E-09	1.00
Rain	3.227E-04	9.982E+02	1.756E-08	1.25
Rain	3.793E-04	9.982E+02	2.851E-08	1.50
Rain	4.370E-04	9.982E+02	4.363E-08	1.75
Rain	4.962E-04	9.982E+02	6.385E-08	2.00
Rain	5.569E-04	9.982E+02	9.029E-08	2.25
Rain	6.195E-04	9.982E+02	1.242E-07	2.50
Rain	1.378E-03	9.982E+02	1.369E-06	5.00
Rain	3.956E-03	9.982E+02	3.236E-05	10.00
Dry snow	2.228E-04	5.439E+02	3.150E-09	0.50
Dry snow	1.692E-03	3.745E+01	9.498E-08	0.75
Dry snow	7.130E-03	8.837E+00	1.677E-06	1.00
Wet snow	2.228E-04	1.345E+03	7.790E-09	1.00
Wet snow	6.800E-04	3.099E+02	5.101E-08	1.25
Wet snow	1.692E-03	1.062E+02	2.693E-07	1.50
Wet snow	3.657E-03	4.728E+01	1.211E-06	1.75
Wet snow	7.130E-03	2.695E+01	5.114E-06	2.00
Wet snow	1.285E-02	1.731E+01	1.922E-05	2.25
Wet snow	2.176E-02	1.221E+01	6.586E-05	2.50
Ice pellet	1.472E-03	9.167E+02	1.532E-06	5.00
Ice pellet	4.276E-03	9.167E+02	3.752E-05	10.00

For dry snow, hydrometeor fall velocities between 0.5 m s^{-1} to 1.0 m s^{-1} were included, representing sizes up to 7 mm and densities below that of ice (Table 2). Fall velocities for wet snow were selected between 1.0 m s^{-1} to 2.5 m s^{-1} for sizes between 0.2 to 21.8 mm. Spherical ice pellets with a density of 916.7 kg/m^3 were also included in the analysis for fall velocities of 5.0 m s^{-1} and 10.0 m s^{-1}. Spherical ~~rain~~ hydrometeors with a density of 998.2 kg/m^3, representing rain, were included for fall velocities from 0.25 m s^{-1} to 10 m s^{-1} for comparison.

The hydrometeor trajectory was derived from the drag force, gravitational force, and buoyancy forces acting on the hydrometeor as it moves through the flow using Lagrangian analysis. A dilute two-phase flow was assumed, where the influence of the hydrometeors on the fluid flow was negligible and hydrometeor interactions including potential hydrometeor coalescence were ignored. Combining these forces gave the net hydrometeor acceleration $\boldsymbol{a}_p$ as a function of the drag coefficient C_D, hydrometeor cross sectional area A_p, density of air ρ_a, relative hydrometeor to air velocity $\boldsymbol{u}_p - \boldsymbol{u}_a$,

Field Code Changed
Field Code Changed
Field Code Changed
Field Code Changed
Field Code Changed

hydrometeor density ρ_p, hydrometeor volume V_p, and acceleration due to gravity g acting in the negative $\hat{\mathbf{z}}$ direction as shown in Eq. (2).

$$\boldsymbol{a}_p = \frac{d\boldsymbol{u}_p}{dt} = -\frac{C_D \rho_a A_p \left|\boldsymbol{u}_p - \boldsymbol{u}_a\right| \left(\boldsymbol{u}_p - \boldsymbol{u}_a\right)}{2\rho_p V_p} + \frac{\left(\rho_a - \rho_p\right) g}{\rho_p} \hat{\mathbf{z}}, \quad (2)$$

The hydrometeors were injected into the flow uniformly at equilibrium with an initial velocity $\boldsymbol{u}_{p1}$ equal to the free-stream wind speed U_w along the $\hat{\mathbf{x}}$ direction and hydrometeor fall velocity U_f in the negative $\hat{\mathbf{z}}$ direction (down).

$$\boldsymbol{u}_{p1} = U_w \hat{\mathbf{x}} - U_f \hat{\mathbf{z}}, \quad (3)$$

~~This ensured that the hydrometeors fell uniformly at equilibrium before they encountered the local flow field around the gauge.~~ In the free-stream region under steady-state conditions, the hydrometeor fall velocity and terminal velocity will be equivalent. Hydrometeor interactions with~~in~~ the inside of the gauge orifice were assumed to be ideal reflections.

The collection efficiency $CE(U_w, U_f)$ for a given free-stream wind speed U_w and hydrometeor fall velocity U_f corresponds to the ratio of the number of hydrometeors collected N_C over the horizontal gauge orifice area A_C to the number of hydrometeors injected from the horizontal injection plane above N_I over the horizontal injection plane area A_I, as shown in Eq. (4).

$$CE(U_w, U_f) = \frac{\frac{N_C}{A_C}}{\frac{N_I}{A_I}} = \frac{N_C A_I}{N_I A_C}, \quad (4)$$

~~The horizontal injection rectangle size of 0.4 m by 5.5 m was sufficiently large to ensure a wide spread of hydrometeors over the gauge orifice. The number of hydrometeors injected per unit area was high (~100000 hydrometeors/rectangle or ~4.5 hydrometeors/cm^2) to ensure high resolution of the collection efficiency estimation.~~

2.3 ~~Overall~~Integral collection efficiency with wind speed

The collection efficiency presented in Sect. 2.2 was for monodispersed hydrometeors with identical size, mass, density and fall velocity. In this section, we define the ~~overall~~integral collection efficiency as that derived over the entire hydrometeor size distribution and associated characteristics (e.g. fall velocity, density and volume) ~~based on observations for liquid and solid precipitation~~.

Field Code Changed

2.3.1 Rainfall

The total precipitation intensity P_{Total} is a function of the hydrometeor size distribution $N_R(D)$, density $\rho_p(D)$, volume $V_p(D)$, fall velocity $U_f(D)$, and density of water ρ_w.

$$P_{Total} = \frac{1}{\rho_w}\int_0^\infty N_R(D)\rho_p(D)V_p(D)U_f(D)\mathrm{d}D, \quad (5)$$

The hydrometeor size distribution (number of hydrometeors per unit size per unit volume) for raindrops $N_R(D)$ can be expressed as a gamma distribution defined by the parameter N_{0R} (m^{-3} $cm^{-1-\mu}$), exponential factor Λ_R (cm^{-1}), exponent μ (unitless), and hydrometeor diameter D (cm) as given by Ulbrich (1983).

$$N_R(D) = N_{0R}D^{\mu}e^{-\Lambda_R D}, \quad (6)$$

Assuming the product of the exponential factor and the maximum hydrometeor diameter is large, the exponential factor can be expressed in terms of the exponent and median volume diameter D_{0R} (cm).

$$\Lambda_R = \frac{3.67+\mu}{D_{0R}}, \quad (7)$$

The median volume diameter is determined based on the rainfall intensity R (mm/hr) and the empirical constants ε and δ for the specific rain type.

$$D_{0R} = \varepsilon R^{\delta}, \quad (8)$$

The value of the exponent μ will be positive or negative depending on the rain type (orographic, thunderstorm, stratiform, or showers), corresponding to a concave up or down distribution when plotted on a $\log(N_R(D))$ versus D plot. Orographic rain with an exponent less than zero corresponds to a concave up distribution with small droplets and low fall speed (Ramana et al., 1959) (Table 3). Thunderstorm rain with a concave down distribution corresponds to large drops and high fall speed (Blanchard, 1953).

The hydrometeor fall velocity for rainfall is given by Beard (1976). At standard air temperature and pressure, the rainfall hydrometeor fall velocity U_f (m s^{-1}) is a function of the equivalent hydrometeor diameter, acceleration due to gravity g, raindrop hydrometeor density (density of water) $\rho_w = 998.2 kg/m^3$, density of air $\rho_a = 1.23 kg/m^3$, dynamic viscosity of air $\eta = 1.79E-5 N\cdot s/m^2$, and surface tension of water $\sigma_w = 0.07199 N/m$.

Table 3. Rainfall parameters for gamma drop size distribution summarized by Ulbrich (1983).

Description	μ	N_0	ε	δ	Source

Orographic rain	-1.03	9.82 x 10^3	0.055	0.28	Ramana et al. (1959)
Thunderstorm rain	1.01	1.24 x 10^6	0.101	0.18	Blanchard (1953)

The ~~overall~~integral collection efficiency is the ratio of the precipitation intensity that is captured by the gauge to that which is falling in the free-stream airflow for a given hydrometeor size distribution, following the approach of Nešpor and Sevruk (1999). The collection efficiency is implicitly dependent on the equivalent hydrometeor diameter through the hydrometeor fall velocity.

$$CE_{\mathrm{R,Overall}} = \frac{\int_0^\infty CE(U_\mathrm{w}, U_\mathrm{f}) D^3 N_R(D) U_\mathrm{f}(D)\,\mathrm{d}D}{\int_0^\infty D^3 N_R(D) U_\mathrm{f}(D)\,\mathrm{d}D}, \quad (9)$$

2.3.2 Snowfall

The total precipitation intensity $P_{\mathrm{S,Total}}$ for snowfall is a function of the hydrometeor size distribution for snowfall $N_\mathrm{S}(D)$, density $\rho_\mathrm{p}(D)$, volume $V_\mathrm{p}(D)$, fall velocity $U_\mathrm{f}(D)$ and density of water ρ_w, integrated over the range of equivalent diameters D.

$$P_{\mathrm{S,Total}} = \frac{1}{\rho_\mathrm{w}} \int_0^\infty N_\mathrm{S}(D) \rho_\mathrm{p}(D) V_\mathrm{p}(D) U_\mathrm{f}(D)\,\mathrm{d}D, \quad (10)$$

Taking the equivalent snowfall diameter as that for a spherical water droplet with the density of water gives the total precipitation intensity integral as a function of the snowfall size distribution. Using this approach, both the size distribution and fall velocities ~~for the~~of snowflakes are defined as a function of the equivalent spherical diameter of water droplets.

$$P_{\mathrm{S,Total}} = \frac{\pi}{6} \int_0^\infty D^3 N_\mathrm{S}(D) U_\mathrm{f}(D)\,\mathrm{d}D, \quad (11)$$

The size distribution for snowflakes $N_\mathrm{S}(D)$ can be expressed by the Gunn and Marshall size distribution (Gunn and Marshall, 1957) as a function of the size distribution parameter N_{0S} ($\mathrm{m^{-1}\,mm^{-1}}$), exponential factor Λ_S ($\mathrm{cm^{-1}}$), and equivalent spherical water drop diameters D (cm) above 0.1 cm.

$$N_\mathrm{S}(D) = N_{0S} e^{-\Lambda_S D}, \quad (12)$$

The size distribution parameter N_{0S} ($\mathrm{m^{-1}\,mm^{-1}}$) and exponential factor Λ_S ($\mathrm{cm^{-1}}$) vary with the precipitation intensity R (mm $\mathrm{h^{-1}}$).

$$N_{0S} = 3.8 \times 10^3 R^{-0.87}, \quad (13)$$

Field Code Changed

$$\Lambda_S = 25.5R^{-0.48}, \quad (14)$$

The median volume diameter D_{0S} (cm) varies with the size distribution slope parameter or precipitation intensity as shown by Atlas (1953).

$$D_{0S} = \frac{3.67}{\Lambda_S}, \quad (15)$$

The fall velocity $U_f(D)$ (cm s^{-1}) for various snowfall types, based on the equivalent spherical diameter of water droplets D (cm), is given by a general power law.

$$U_f(D) = aD^b, \quad (16)$$

The fall velocity power law coefficients for dendrites, rimed dendrites, and a mixture of dendrites and aggregates of plates is summarized in Table 4 based on the work of Langleben (1954).

Table 4. Snowfall fall velocity parameters with power law formulation for equivalent water droplet diameter.

Description	*a*	*b*	Source
Dendrites	178	0.372	Langleben (1954)
Rimed dendrites	210	0.283	Langleben (1954)
Mixture of dendrites and aggregate of plates	366	0.611	Langleben (1954)

The ~~overall~~integral collection efficiency at a given wind speed is the ratio of the precipitation intensity that is captured by the gauge to that which is falling in the free-stream airflow for a given crystal habit and size distribution. As with that for rainfall, the collection efficiency is implicitly dependent on the equivalent hydrometeor diameter through the hydrometeor fall velocity.

$$CE_{S,Overall} = \frac{\int_0^\infty CE(U_w, U_f) D^3 N_S(D) U_f(D) \mathrm{d}D}{\int_0^\infty D^3 N_S(D) U_f(D) \mathrm{d}D}, \quad (17)$$

3 Modelling results

Commented [JH4]: Sect. 3 added from Part I

3.1 Numerical modelling

Computational fluid dynamics simulations that included the time-averaged effects of flow turbulence were run for free-stream wind speeds between 0 and 10 m s^{-1} for the unshielded Geonor precipitation gauge. Results for the 1 m s^{-1} case are shown in Fig. 2. The flow is diverted upward as it passes over the leading edge of the gauge, with recirculation of the airflow within the gauge orifice (Fig. 2~~a~~). This general velocity profile has been well established in previous studies (Thériault et al., 2012;Colli et al., 2016a;Baghapour et al., 2017). ~~The upward z velocity profile directly above the leading edge of the gauge orifice shows a sharp increase from zero up to a peak value of 0.95 m s^{-1} roughly 7.6 mm above the orifice, and decreases with height above this point (Fig. 2b).~~

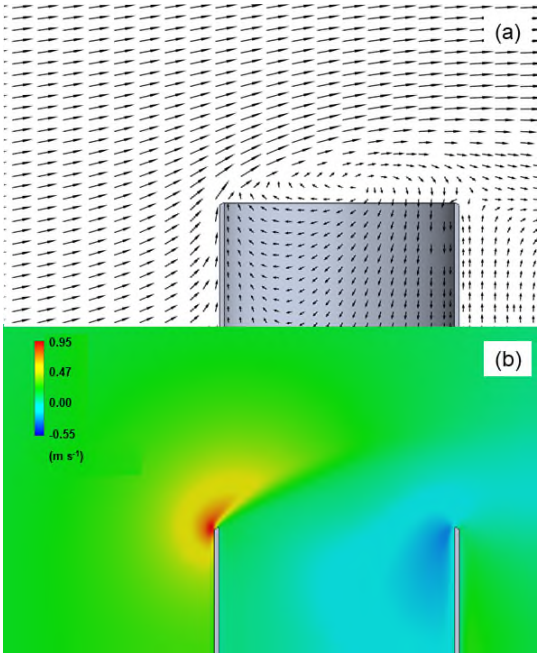

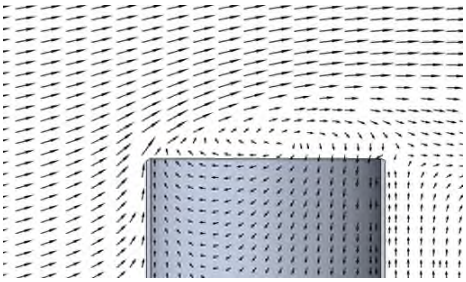

Figure 2. Air velocity around Geonor gauge for 1 m s^{-1} free-stream horizontal wind speed represented by ~~(a)~~ velocity magnitude and direction ~~and (b) upward z velocity~~.

335

To validate the CFD model used in the present study, normalized velocities along the gauge centerline u^* (normalized by the free-stream wind speed) as a function of the normalized height above the gauge orifice z^* (normalized by the orifice diameter) ~~Peak velocities along the gauge centerline, normalized by the free-stream wind speed u^*,~~ are compared with results from previous studies for wind speeds of 1 m s^{-1} and 10 m s^{-1} in Fig. 3. The peak normalized velocities are 2 % lower than the 340 Baghapour et al. (2017) k-ω SST model at 1 m s^{-1} wind speed (Fig. 3a) and within 1 % at 10 m s^{-1} wind speed (Fig. 3b). Larger differences in peak normalized velocity, within 9 %, are observed relative to the Colli (2016a) k-ω SST model results at 1 m s^{-1} wind speed (Fig. 3a).

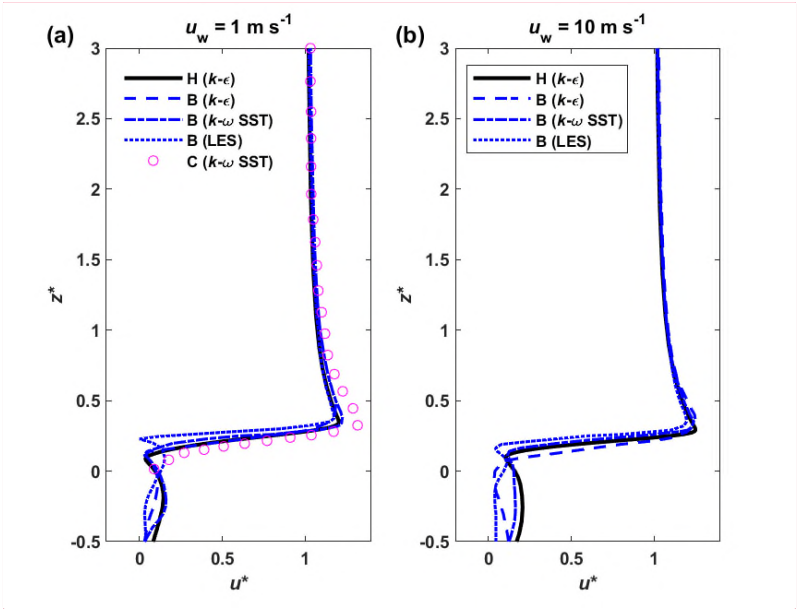

Commented [JH5]: Replaced

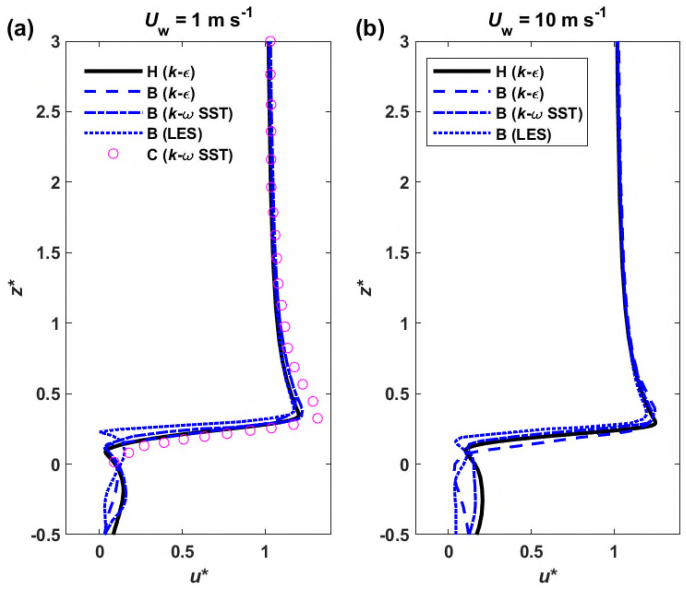

Figure 3. Gauge centerline results comparison above gauge orifice for present model (H k-ε), Baghapour et. al. (2017) k-ε model (B k-ε), Baghapour et. al. (2017) k-ω shear stress tensor model (B k-ω SST), Baghapour et. al. (2017) LES model (B LES), and Colli et. al. (2016a) k-ω shear stress tensor model (C k-ω SST) for normalized free-stream velocity (u*) with (a) 1 m s^{-1} wind speed U_w and (b) 10 m s^{-1} wind speed U_w.

For visualization purposes, hydrometeor trajectories are illustrated for the 3 m s^{-1} wind speed case with fall velocities of 0.5 m s^{-1}, 1.0 m s^{-1}, 1.5 m s^{-1} and 2.0 m s^{-1} in Fig. 4. As the fall velocity increases, the hydrometeor approach angle from the horizontal increases, based on the relative magnitudes of the wind speed and fall velocity. For the 2.0 m s^{-1} hydrometeor fall velocity, it is apparent that the hydrometeor trajectories experience little change due to the local airflow around the gauge (Fig. 4d). For lower fall velocities, the deflection due to the updraft around the leading edge of the gauge is more apparent, with the 0.5 m s^{-1} fall velocity hydrometeors closely coupled to the flow upward and over the gauge, with a few hydrometeors drawn in at the back side of the gauge orifice (Fig. 4a). For each of the hydrometeor injections, the same horizontal spacing of hydrometeors is present prior to encountering the local airflow around the gauge. The number of hydrometeors captured is reduced for lower hydrometeor fall velocities at the same wind speed. At 3 m s^{-1} wind speed, rainfall hydrometeors with 0.25 m s^{-1} hydrometeor fall velocity are all carried over the gauge, corresponding to a collection efficiency of zero (not shown).

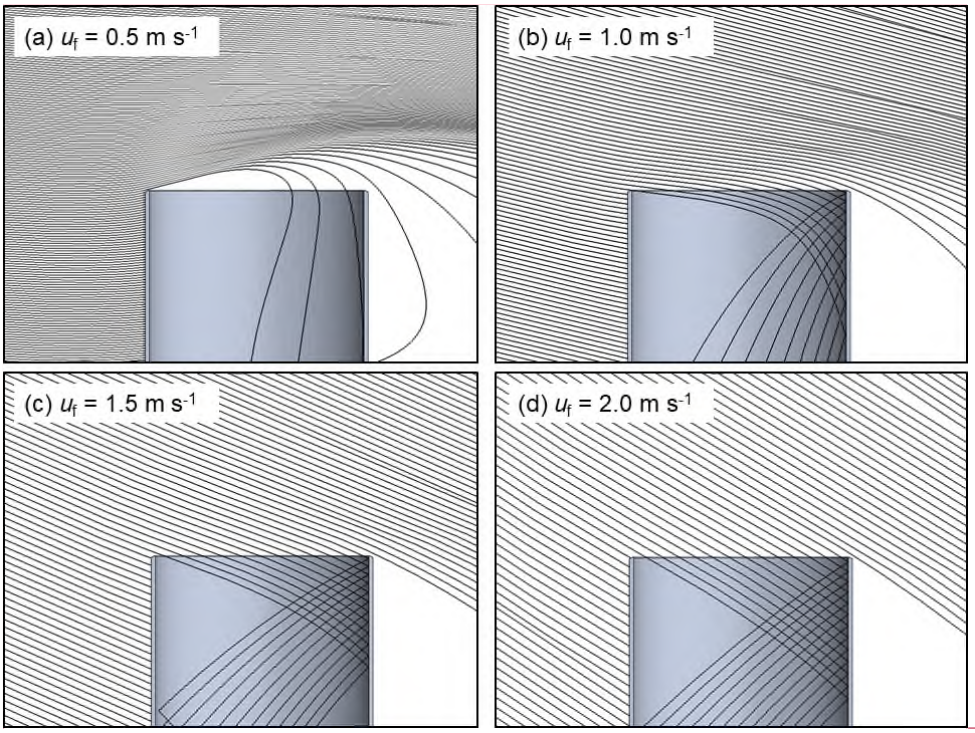

Commented [JH6]: Replaced

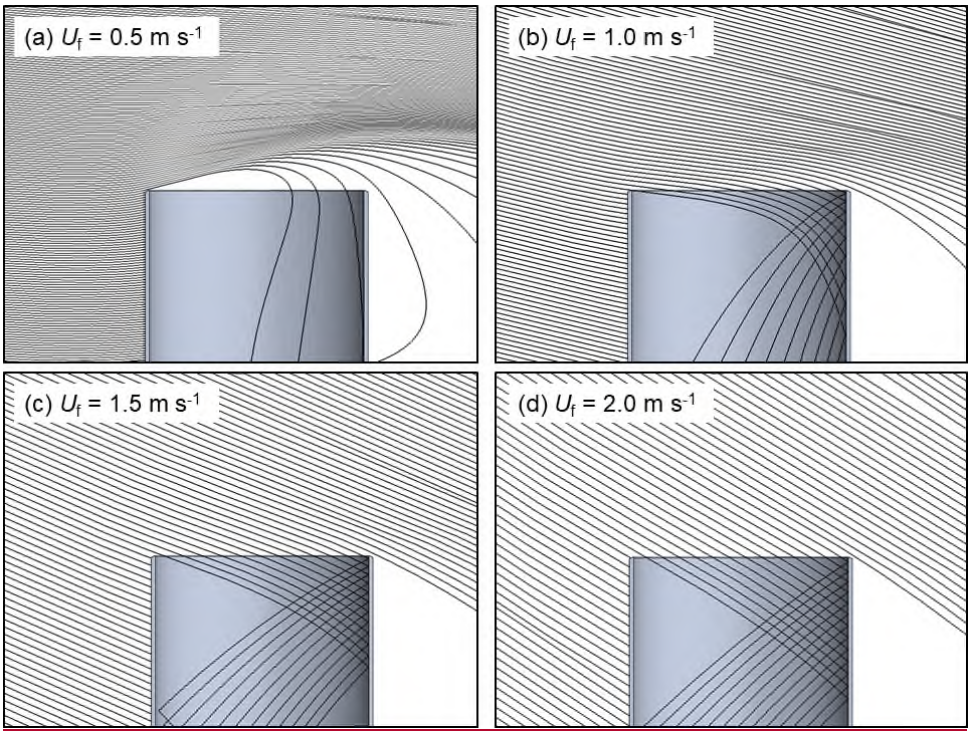

Figure 4. Flow simulation results showing hydrometeor trajectories for 3 m s^{-1} free-stream wind velocity with rain hydrometeor fall velocity of (a) 0.5 m s^{-1}, (b) 1.0 m s^{-1}, (c) 1.5 m s^{-1}, and (d) 2.0 m s^{-1}.

3.2 Collection efficiency dependency on wind speed and hydrometeor fall velocity

The numerical results demonstrate a clear dependence on the hydrometeor fall velocity (Fig. 5). Hydrometeors with higher fall velocities exhibit increased collection efficiency, and the collection efficiency tends to decrease with increasing wind speed. Rain, dry snow, and wet snow hydrometeors with 1.0 m s^{-1} fall velocity exhibit a similar collection efficiency decrease with increasing wind speed, despite differences in diameter, density, and mass. For rain and ice pellet hydrometeors with 5.0 m s^{-1} fall velocities, the results are close to 1 and nearly identical at all wind speeds, irrespective of differences in density. Here, the circles for rain overlap the squares for ice pellets in Fig. 5. Rain and wet snow with identical fall velocities between 1.0 m s^{-1}

and 2.5 m s^{-1} also exhibit similar results for wind speeds under 5 m s^{-1}. Above 5 m s^{-1} wind speed, the collection efficiency for rain is slightly elevated above that for wet snow. For dry snow hydrometeors with fall velocities between 0.5 m s^{-1} and 1.0 m s^{-1}, there is good agreement with the corresponding rain hydrometeors for horizontal wind speeds up to about 3 m s^{-1} ~~wind speed~~. Above this wind speed, the 0.5 m s^{-1} dry snow hydrometeors exhibit good agreement with rain hydrometeors, while the collection efficiency for 1.0 m s^{-1} dry snow hydrometeors decreases more rapidly with wind speed relative to rain hydrometeors with the same fall velocity. Collection efficiency differences across all hydrometeor types with identical fall velocities are within 0.18, with root mean square differences of 0.05, over all wind speeds and hydrometeor fall velocities studied.

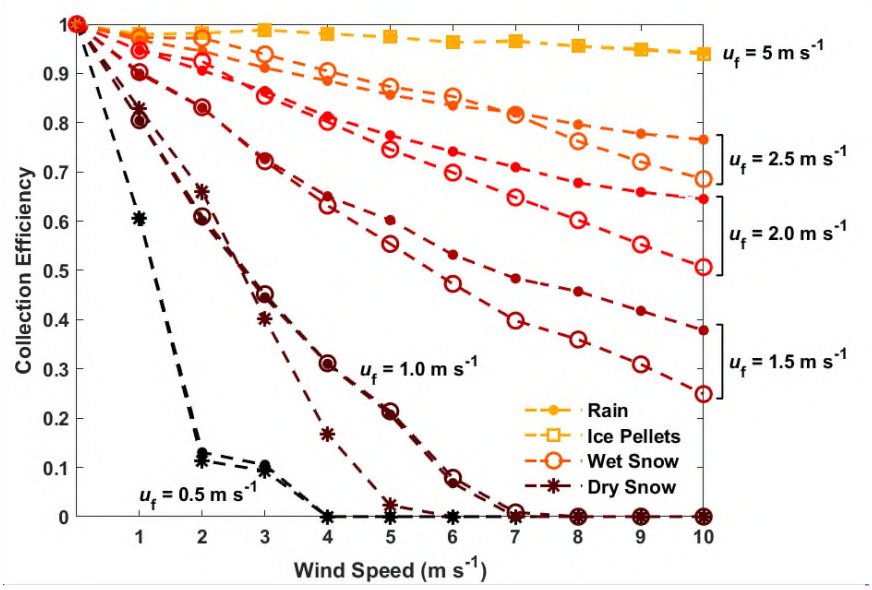

Commented [JH7]: Replaced

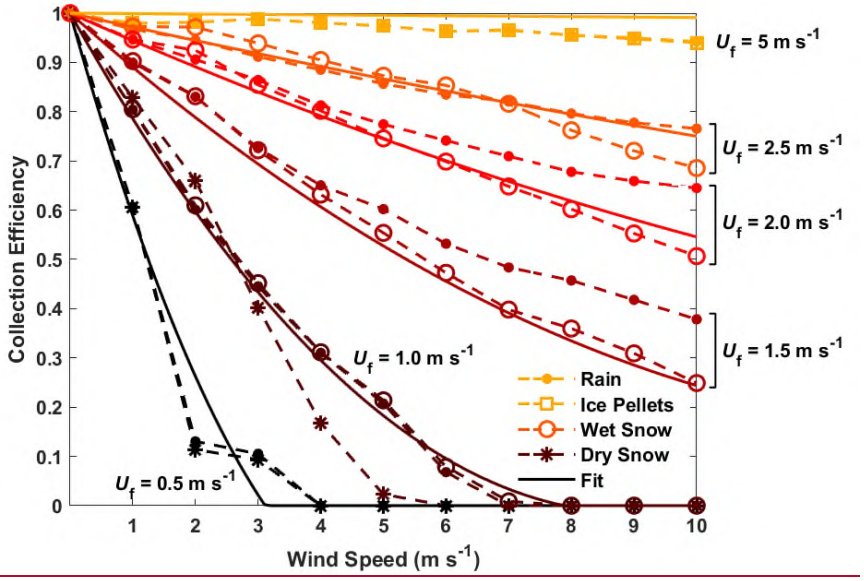

Figure 5. Flow simulation results for Geonor unshielded gauge collection efficiency based on wind speed and hydrometeor fall velocity for rain, ice pellets, wet snow, ~~and~~ dry snow, and CFD transfer function.

3.3 ~~Empirical collection efficiency expression~~CFD transfer function

The simulation results demonstrate that the collection efficiency is dependent on the free-stream wind speed U_w and hydrometeor fall velocity U_f . ~~An empirical expression for the collection efficiency~~The CFD transfer function, $CE_{CFD}(U_w, U_f)$, is presented based on a polynomial fit to wind speed and an exponential hydrometeor fall velocity dependence, with both velocities having units of m s^{-1}.

$$CE_{CFD}(U_w, U_f) = 1 - b_1 U_w e^{-b_2 U_f} + b_3 U_w^2 e^{-b_4 U_f}, \quad (18)$$

This expression was selected due to its ability to capture the nonlinearity in the collection efficiency up to 10 m s^{-1} wind speed, as well as the nonlinear fall velocity dependence with collection efficiencies approaching 1 for higher fall velocities. Table 5 shows the best-fit coefficients (RMSE of 0.03) from a combined nonlinear regression for dry snow (0.5 m s^{-1} and 0.75 m s^{-1} fall velocities), wet snow (1.0 m s^{-1}, 1.25 m s^{-1}, … , 2.5 m s^{-1} fall velocities), and rain (5 and 10 m s^{-1} fall velocities). A single

CFD curve was used for each fall velocity in the fit to ensure that the transfer function was unbiased over the entire range of fall velocities studied.

Table 5. Non-linear regression fit parameters, standard errors (SE), and units for the Geonor unshielded gauge collection efficiency as a function of wind speed and hydrometeor fall velocity with RMSE = 0.0302 and R^2 = 0.989.

Coefficient	Value	SE	Units
b_1	0.908	0.048	s m^{-1}
b_2	1.387	0.037	s m^{-1}
b_3	0.143	0.031	s^2 m^{-2}
b_4	2.422	0.167	s m^{-1}

A wind speed threshold U_{wc} is defined above which the collection efficiency is zero for a given maximum cutoff hydrometeor fall velocity U_{fc}. This was derived from Eq. (18) by solving for the roots where the collection efficiency is zero using the quadratic formula. Conversely, this expression gives the hydrometeor fall velocity below which the collection efficiency will be zero for a given wind speed.

$$U_{wc} = \frac{b_1}{2b_3}\exp\left[\left(b_4 - b_2\right)U_{fc}\right] - \frac{\sqrt{b_1^2\exp\left(-2b_2U_{fc}\right) - 4b_3\exp\left(-b_4U_{fc}\right)}}{2b_3\exp\left(-b_4U_{fc}\right)}, \quad (19)$$

Fig. ~~6~~ 5 shows ~~a~~ the comparison of the ~~results from the empirical expression~~CFD transfer function with the CFD results. For hydrometeor fall velocities above 5.0 m s^{-1}, the collection efficiency expression is ~~slightly over predicted (up to 0.05) by the expression~~ within -0.13 and 0.10 of CFD results over all hydrometeor types. For fall velocities between 1.~~0~~25 to 2.5 m s^{-1}, the fit is within ±0.06 over all wind speeds. For fall velocities of 0.25 m s^{-1} to 1.0 m s^{-1}, the fit captures the rapid decrease in collection efficiency with wind speed well overall, with a maximum difference of ~~0.15~~ 0.16 for dry snow at ~~2~~ 5 m s^{-1} wind speed. The CFD transfer function captures well the collection efficiency trends for ~~across specific~~the different hydrometeor types, with RMSE values of ~~the RMSE of the CFD transfer function is~~ 0.04 for rain, 0.02 for ice pellets, 0.02 for wet snow, and 0.05 for dry snow.

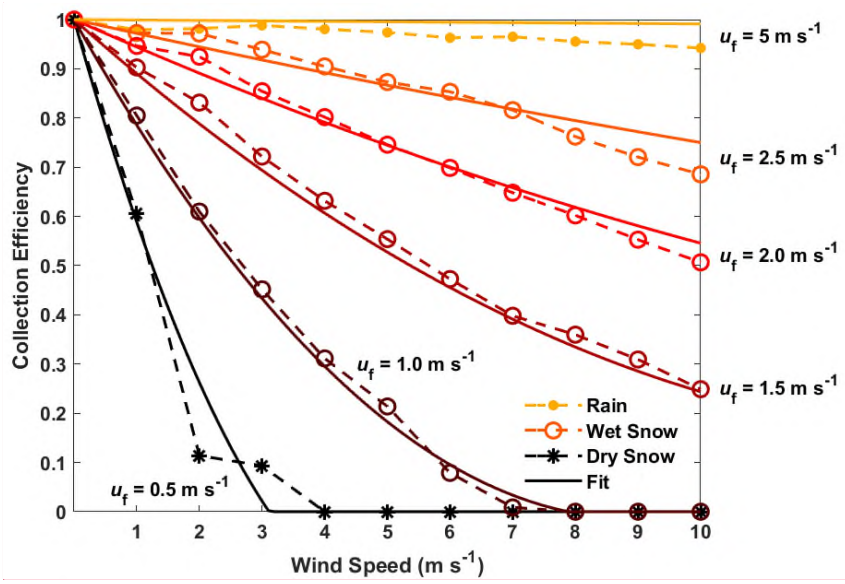

Figure 6. Geonor unshielded gauge collection efficiency results for rain, wet snow, dry snow, and exponential fit model based on wind speed and hydrometeor fall velocity.

Fig. 7 6 shows the empirical collection efficiency expressionCFD transfer function dependence with fall velocity. For a given wind speed, the collection efficiency increases nonlinearly with hydrometeor fall velocity. For fall velocities above 3 m s^{-1} the collection efficiency is close to 1. The collection efficiency rapidly decreases as the fall velocity is reduced, particularly below 2.5 m s^{-1} fall velocity. Increasing the wind speed decreases the collection efficiency. The fall velocity where the collection efficiency is zero illustrates the fall velocity cutoff given by Eq. (19). Hydrometeors at or below this fall velocity will not be captured by the gauge. As the wind speed increases, the fall velocity cutoff increases, reaching 1.1 m s^{-1} at 9 m s^{-1} wind speed.

Commented [JH8]: Deleted

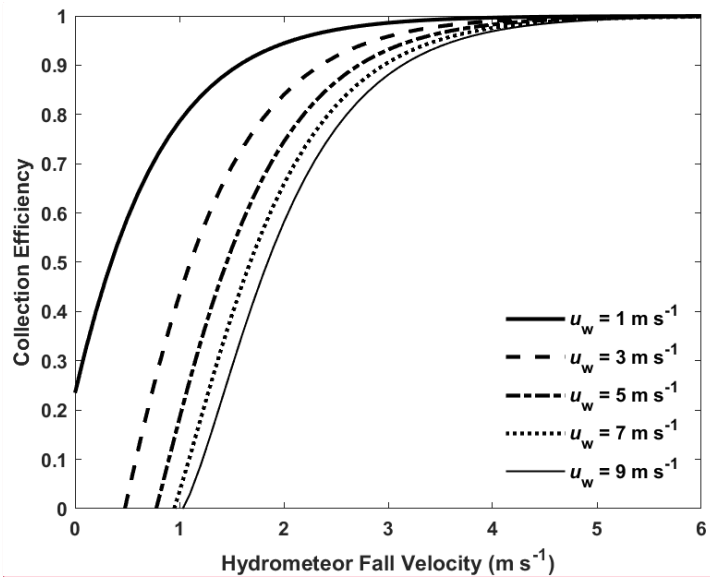

Commented [JH9]: Replaced

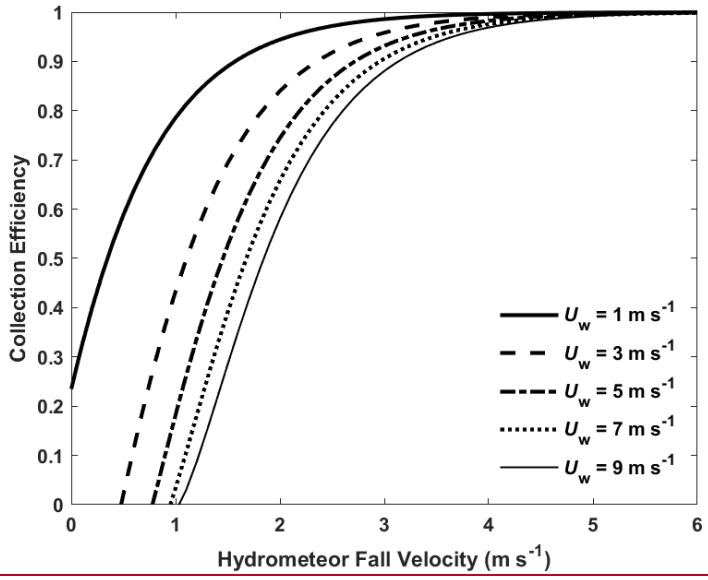

Figure ~~7~~6. Geonor unshielded gauge collection efficiency for exponential fit model with hydrometeor fall velocity and wind speed.

3.4 ~~Overall~~ Integral collection efficiency

~~3.4.1 Comparison with previous studies~~

~~The overall integral collection efficiency for a distribution of hydrometeors is obtained by integrating the ratio of the precipitation intensity captured by the gauge to that which is falling in air over the range of hydrometeor sizes present. The empirical expression~~CFD transfer function ~~(Eq. 18) captures the gauge collection efficiency for a given wind speed and hydrometeor fall velocity. A hydrometeor size distribution with intercept $N_{0S} = 5\times10^{6}\ \mathrm{m}^{-4}$ and slope $\Lambda_S = 1\mathrm{mm}^{-1}$ for hydrometeor sizes between 0.25 mm to 20 mm was used for dry snow and wet snow for comparison with the work of Colli et al. (2016b). Overall Integral collection efficiency results between the two models show good agreement (Fig. 8). For dry snow, the overall integral collection efficiency decreases more gradually with wind speed in the present study than the Colli et al. (2016b) results, with collection efficiency values up to 0.18 higher at 3 m s^{-1} wind speed using the present model. For wet snow, the results of Colli et al. (2016b) show a nonlinear decrease in collection efficiency above 5 m s^{-1} wind speed that is not~~

apparent in the results from the present study. As a result, the present study predicts up to 0.16 higher collection efficiency at 8 m s^{-1} wind speed.

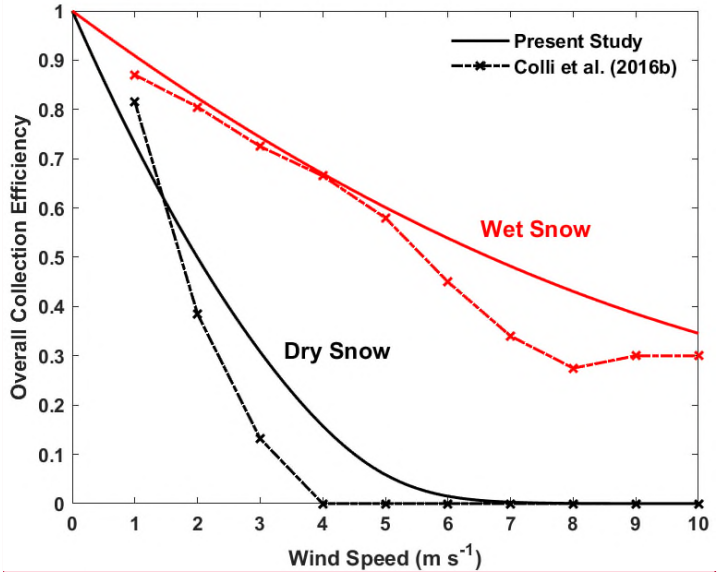

Figure 8. Overall Integral Geonor unshielded gauge collection efficiency with wind speed for present study and Colli et al. (2016b) *k-ω* SST model for dry snow and wet snow with Colli et al. (2016b) size distribution.

Commented [JH10]: Moved

3.4.1 Wind speed dependence

For each hydrometeor type and precipitation intensity, the overall integral collection efficiency (Eqs. 9 and 17) was derived for wind speeds from 0 to 10 m s^{-1} using the empirical expression for collection efficiencyCFD transfer function (Eq. 18) based solely on wind speed and hydrometeor fall velocity. The collection efficiency, derived using the fall velocityCFD transfer function, decreases nonlinearly with wind speed, decreasing more rapidly at lower wind speeds and more gradually at higher wind speeds above approximately 5 m s^{-1} (Fig. 97). A wide range of overall integral collection efficiency results with wind speed is apparent, depending on the hydrometeor type and precipitation intensity.

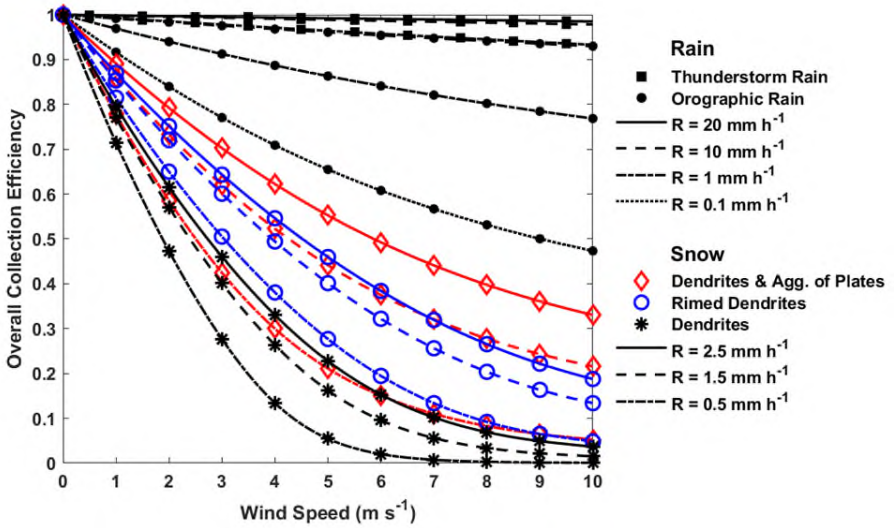

Figure ~~9~~7. ~~Overall~~ Integral Geonor unshielded gauge collection efficiency with wind speed for thunderstorm rain at 20 mm h^{-1}, 10 mm h^{-1}, and 1 mm h^{-1} precipitation intensities (R); orographic rain at 10 mm h^{-1}, 1 mm h^{-1}, and 0.1 mm h^{-1} precipitation intensities (R); and aggregates of plates, rimed dendrites, and dendrites at 2.5 mm h^{-1}, 1.5 mm h^{-1}, and 0.5 mm h^{-1} precipitation intensities (R).

Lower ~~overall~~ integral collection efficiencies are observed for snowfall relative to orographic and thunderstorm rain. Across snowfall types, a wide range of integral collection efficiency values are apparent. Dendrites show the greatest nonlinearity with wind speed and the lowest integral collection efficiency, with the latter ~~The overallintegral collection efficiency for dendrites with 0.5 mm h^{-1} precipitation intensity~~ decreasinges to 0.01 at 6.7 m s^{-1} wind speed and 0.5 mm h^{-1} precipitation intensity.~~, exhibiting the lowest overallintegral collection efficiency and greatest nonlinearity with wind speed.~~ The ~~overall~~integral collection efficiency continues to decrease with increasing wind speed, remaining small, but non-zero, up to 10 m s^{-1} wind speed. For 1.5 mm h^{-1} and 2.5 mm h^{-1} intensities, ~~overall~~integral collection efficiencies are higher, with the magnitude of the increase varying with the wind speed. It is important to note the more gradual decrease in integral collection efficiency for wind speeds above ~6 m s^{-1} compared with the results in Fig. ~~6~~5 for a given hydrometeor fall velocity. The integral collection efficiency includes the contribution from a range of hydrometeor sizes, including larger hydrometeors with higher fall velocities that are still able to be captured by the gauge, providing small but non-zero integral collection efficiencies. For comparison, integral collection efficiency results were computed for dry snow and wet snow using the same hydrometeor size distribution parameters as Colli et al. (2016b) for sizes between 0.25 mm to 20 mm. The results from the different models show good agreement (Fig. 8). For dry snow, the integral collection efficiency decreases more gradually with wind speed in

the present study than the Colli et al. (2016b) results, with collection efficiency values up to 0.18 higher at 3 m s^{-1} wind speed using the present model. For wet snow, the results of Colli et al. (2016b) show a nonlinear decrease in collection efficiency above 5 m s^{-1} wind speed that is not apparent in the results from the present study. As a result, the present study predicts up to 0.16 higher collection efficiency at 8 m s^{-1} wind speed.

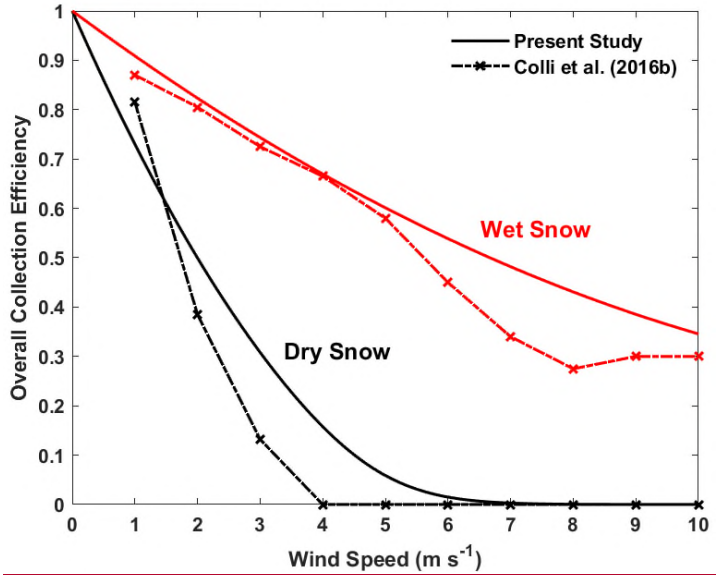

Figure 8. Integral Geonor unshielded gauge collection efficiency with wind speed for present study and Colli et al. (2016b) *k-ω* SST model for dry snow and wet snow with Colli et al. (2016b) size distribution.

~~Across snowfall types, a wide range of overallintegral collection efficiency values are apparent. Dendrites show the lowest overallintegral collection efficiency, while dendrites and aggregates of plates with 2.5 mm h^{-1} precipitation intensity show a much higher overallintegral collection efficiency of 0.55 at 5 m s^{-1} wind speed. Dendrites and aggregates of plates also show the largest spread in overallintegral collection efficiency with precipitation intensity, with the overallintegral collection efficiency between 0.21 and 0.55 for 0.5 mm h^{-1} and 2.5 mm h^{-1} precipitation intensities, respectively, at 5 m s^{-1} wind speed. This spread decreases at higher wind speeds as the overallintegral collection efficiency for 0.5 mm h^{-1} decreases more gradually. Rimed dendrites provide intermediate values, above those for dendrites and below those for dendrites and aggregates of plates, for 2.5 mm h^{-1} precipitation intensity.~~

~~Orographic and thunderstorm rain exhibit overall~~integral ~~collection efficiencies greater than those for snow. The overall~~integral ~~collection efficiencies for orographic rain at 5 m s^{-1} wind speed and 0.1 mm h^{-1}, 1 mm h^{-1} and 10 mm h^{-1} precipitation intensities are 0.66, 0.86, and 0.96, respectively. For thunderstorm rain at 5 m s^{-1} wind speed, the overall~~integral ~~collection efficiencies are 0.96, 0.98, and 0.99 at 1 mm h^{-1}, 10 mm h^{-1}, and 20 mm h^{-1} precipitation intensities, respectively.~~

3.4.2 Precipitation intensity dependence

Using the CFD transfer function, i~~I~~ntegral collection efficiencies were derived for 0.5 mm h^{-1}, 1.5 mm h^{-1}, and 2.5 mm h^{-1} precipitation intensities for three different snowfall types, between 0.1 mm h^{-1} and 10 mm h^{-1} for orographic rain, and between 1 mm h^{-1} and 10 mm h^{-1} for thunderstorm rain. ~~–~~The results are shown in Fig. 9 for selected ~~The overall~~integral ~~collection efficiency was derived for each precipitation type, precipitation intensity, and~~ wind speeds (1 m s^{-1}, 3 m s^{-1}, and 6 m s^{-1}). ~~Fig. 10~~ 9 shows how the overall~~integral~~ collection efficiency varies with precipitation intensity for given wind speeds and hydrometeor types. Overall~~Integral collection efficiencies were derived for 0.5 mm h^{-1}, 1.5 mm h^{-1}, and 2.5 mm h^{-1} precipitation intensities for three different snowfall types, between 0.1 mm h^{-1} and 10 mm h^{-1} for orographic rain, and between 1 mm h^{-1} and 10 mm h^{-1} for thunderstorm rain.~~

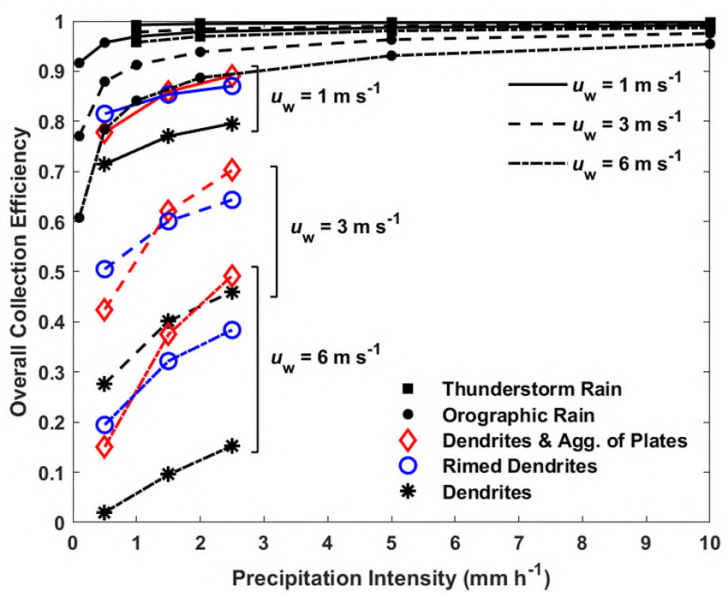

Commented [JH11]: Replaced

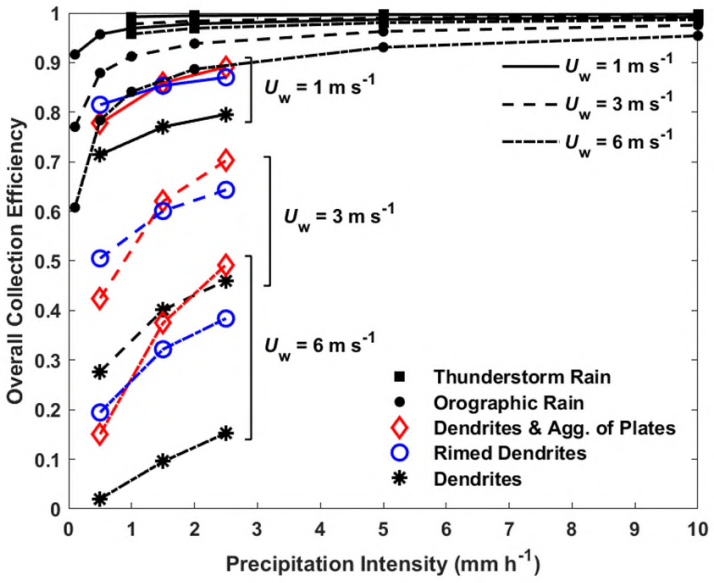

Figure ~~10~~9. ~~Overall~~Integral Geonor unshielded gauge collection efficiency with precipitation intensity for rainfall and snowfall types at 1 m s^{-1}, 3 m s^{-1}, and 6 m s^{-1} wind speeds.

~~Overall~~Integral collection efficiencies increase with precipitation intensity and decrease with wind speed. For thunderstorm rain at 3 m s^{-1} wind speed, the ~~overall~~integral collection efficiency increases from 0.97 to 0.99 when the precipitation intensity increases from 1 mm h^{-1} to 10 mm h^{-1}. For orographic rain, a sharp decrease in the ~~overall~~integral collection efficiency is apparent with decreasing precipitation intensity below 1 mm h^{-1}. ~~At 3 m s^{-1} wind speed, the overall~~integral ~~collection efficiency for orographic rain increases from 0.77 at 0.1 mm h^{-1}, to 0.91 at 1 mm h^{-1}, and 0.97 at 10 mm h^{-1}. Increasing the wind speed reduces the overall~~integral ~~collection efficiency, with the value for orographic rain decreasing from 0.97 at 1 m s^{-1} wind speed, to 0.91 at 3 m s^{-1} wind speed, and 0.84 at 6 m s^{-1} wind speed.~~

For all snowfall types, the ~~overall~~integral collection efficiency is shifted to lower values relative to rain. ~~The overall~~integral ~~collection efficiency is 0.62, 0.60, and 0.40 for dendrites and aggregates of plates, rimed dendrites, and dendrites at 3 m s^{-1} wind speed and 1.5 mm h^{-1} precipitation intensity, respectively.~~ The ~~overall~~integral collection efficiency increases with precipitation intensity from 0.42 at 0.5 mm h^{-1} to 0.70 at 2.5 mm h^{-1} for dendrites and aggregates of plates at 3 m s^{-1} wind

speed. Increasing the wind speed to 6 m s^{-1} further decreases the ~~overall~~integral collection efficiency from 0.15 at 0.5 mm h^{-1} to 0.49 at 2.5 mm h^{-1}.

For dendrites and aggregates of plates, rimed dendrites, and dendrites, ~~overall~~integral collection efficiencies are within 0.09 to 0.10 of one another for 0.5 mm h^{-1} precipitation intensities at 1 m s^{-1} wind speed. This range increases to 0.17 for 0.5 mm h^{-1} precipitation intensity and 0.34 for 2.5 mm h^{-1} precipitation intensity at 6 m s^{-1} wind speed. This provides an estimate of the overall variability in integral collection efficiency due to crystal habit if the precipitation intensity, wind speed, and the occurrence of snowfall are all known, but not the specific snowfall type. In cases where only the precipitation intensity and wind speed is known, and the hydrometeor phase (rainfall or snowfall) and type is uncertain, the range of possible ~~overall~~integral collection efficiencies grows dramatically. For example, at 6 m s^{-1} wind speed, the ~~overall~~integral collection efficiencies for rain exceed 0.75, while that for dendrites is below 0.16; hence, the catch efficiency in this case can vary by ~ 0.74 depending on the hydrometeor phase and type.

3.4.3 Hydrometeor fall velocity dependence

Fig. ~~11~~ 10 shows the ~~overall~~integral collection efficiency as a function of hydrometeor fall velocity for each precipitation type (thunderstorm rain, orographic rain, dendrites and aggregates of plates, rimed dendrites, and dendrites), precipitation intensity (0.1 to 20 mm h^{-1} for rainfall and 0.5 to 2.5 mm h^{-1} for snowfall), and wind speed (1 m s^{-1}, 3 m s^{-1}, and 6 m s^{-1}) shown previously in Fig. ~~10~~9. Here, the fall velocity at the median volume diameter is used as an estimate for the fall velocity distribution. The results take a similar form to that of the ~~empirical expression for collection efficiency~~CFD transfer function shown in Fig. ~~7~~6, with collection efficiencies increasing nonlinearly with hydrometeor fall velocity for a given wind speed. Dendrites, with the lowest fall velocity, exhibit the lowest ~~overall~~integral collection efficiency. Rimed dendrites and dendrites and aggregates of plates with higher fall velocity exhibit higher collection efficiency. In this fall velocity range below 1.5 m s^{-1}, the collection efficiency rapidly increases approximately linearly with fall velocity. For orographic rain and thunderstorm rain, ~~—~~with even higher fall velocity, the ~~overall~~integral collection efficiency nonlinearly approaches 1. As wind speeds increase from 1 m s^{-1} to 6 m s^{-1}, collection efficiencies for all precipitation types are shifted down at the lower end of the fall velocity spectrum below 2 m s^{-1} and still converge to 1 at higher fall velocities, close to 5 m s^{-1}.

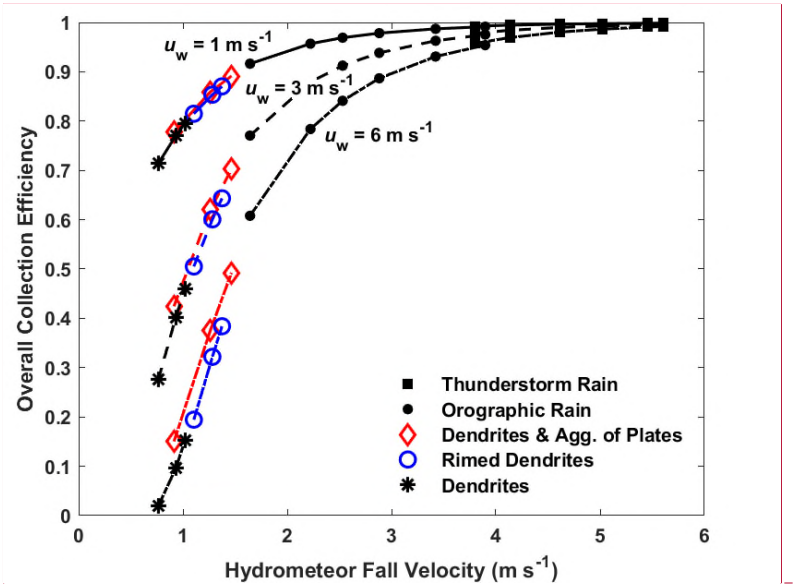

Commented [JH12]: Replaced

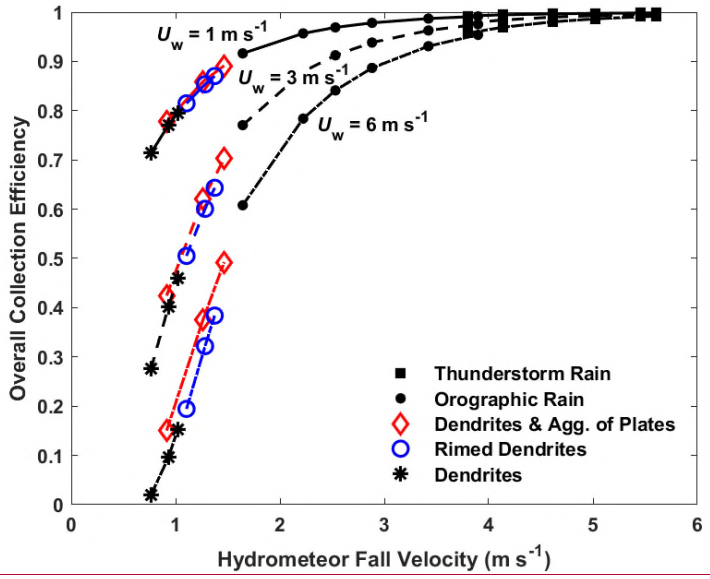

Figure ~~11~~10. ~~Overall~~Integral Geonor unshielded gauge collection efficiency with hydrometeor fall velocity at median volume diameter for rainfall and snowfall types at 1 m s^{-1}, 3 m s^{-1}, and 6 m s^{-1} wind speeds.

For snowfall, the ~~overall~~integral collection efficiency difference across dendrites, rimed dendrites, and dendrites and aggregates of plates is less than 0.06 for 0.5 mm h^{-1}, 1.5 mm h^{-1}, and 2.5 mm h^{-1} precipitation intensities at 6 m s^{-1} wind speed, and within 0.03 for the same precipitation intensities at 3 m s^{-1} wind speed. For rainfall, the ~~overall~~integral collection efficiency difference is less than 0.01 at 3.8 m s^{-1} fall velocity, where orographic rain and thunderstorm rain overlap. Orographic rain exhibits median volume diameter fall velocities between 1.6 m s^{-1} to 3.9 m s^{-1} for precipitation intensities from 0.1 mm h^{-1} to 10 mm h^{-1}. Thunderstorm rain exhibits median volume diameter fall velocities between 3.8 m s^{-1} to 5.6 m s^{-1} for precipitation intensities from 1 mm h^{-1} to 20 mm h^{-1}.

24 Experimental Mmethod

42.1 Instrumentation

Experimental measurements were performed in conjunction with SPICE over the 2013/14 and 2014/15 winter periods (November 1 to April 30) at the Centre for Atmospheric Research Experiments (CARE) site in Egbert, Ontario, Canada. Measurements of precipitation accumulation were performed using 600 mm capacity Geonor T-200B3 gauges in unshielded and reference DFAR configurations. Both gauges were securely mounted on concrete foundations to limit wind-induced vibrations. The performance of these gauges was confirmed by full-scale field verifications at the start and end of testing, with annual maintenance to inspect, clean, level, and recharge each gauge. The gauges were charged with a mixture of antifreeze (60% methanol and 40% propylene glycol) and oil (Esso Bayol 35 in 2013/14, discontinued; Exxon Mobil Isopar M in 2014/15).

Measurements of precipitation occurrence were obtained using a Thies Laser Precipitation Monitor (LPM) installed inside the inner fence of the DFAR. Wind speed and direction measurements at 2 m gauge height were performed with a Vaisala WS425 ultrasonic wind sensor adjacent to the unshielded gauge. Temperature was measured with a Yellow Springs International model 44212 thermistor in an aspirated Stevenson screen. Further details are available in the SPICE final report (Nitu et al., 2018).

42.2 Sampling, quality control, and precipitation event selection

The instruments were sampled using a Campbell Scientific CR3000 data logger. For each Geonor T-200B3 precipitation gauge, the frequency and precipitation accumulation for each of the three transducers was reported at 6-second intervals, the latter computed from the former using manufacturer-provided calibration coefficients. Minutely measurements of precipitation occurrence from the Thies LPM were recorded. The scalar average wind speed and vector average wind direction were recorded over 1-minute intervals. Based on SPICE procedures, these data were processed using a format check to replace missing data with null values, a range check to identify and remove outliers outside the manufacturer-specified output thresholds, a jump filter to remove spikes exceeding maximum point-to-point variation thresholds, and a Gaussian filter to smooth out high frequency noise in Geonor precipitation accumulation measurements (Nitu et al., 2018). Periods of instrument maintenance and power outages were removed from the analysis. The Geonor accumulation data were aggregated to 1-minute intervals for subsequent analysis.

Precipitation events were identified during both measurement periods using the SPICE event selection procedure (Nitu et al. 2018). These events were defined as 30-minute periods with at least 0.25 mm of precipitation recorded by the reference DFAR precipitation gauge and at least 60% precipitation occurrence reported by the Thies LPM. The use of the LPM as a secondary confirmation of precipitation occurrence minimizes the likelihood of events with false precipitation due to dumps of snow or ice into the gauge, wind induced vibrations, or other factors. Following the approach of Kochendorfer (2018), a minimum 0.075 mm accumulation threshold was applied for the unshielded gauge to ensure that measurements exceeded the gauge uncertainty and that derived collection efficiency values were reliable. The 30-minute event duration was chosen to be

sufficiently long to reduce noise and ensure high confidence in measured parameters and sufficiently short to avoid the influence of diurnal temperature variations, while also providing a larger number of events for analysis relative to longer durations. Note that unless otherwise stated, all precipitation events referred to hereafter are 30-minute events derived using the above approach.

42.3 POSS fall velocity and precipitation type

The POSS is a small upward-facing bistatic X band radar capable of measuring the precipitation fall velocity based on the Doppler frequency shift of the received signal (Canada, 1995;Sheppard, 1990, 2007;Sheppard et al., 1995;Sheppard and Joe, 1994, 2000, 2008). During periods of precipitation, the POSS outputs both the mean and mode received signal frequency derived from the Doppler frequency spectrum over the previous minute. The mean precipitation fall velocity $U_{\text{f\_mean}}$ is estimated from the transmitted wavelength λ and the mean frequency f_{mean} of the measured Doppler power density spectrum for falling precipitation hydrometeors.

$$U_{\text{f\_mean}} = \frac{f_{\text{mean}}\lambda}{2}, \qquad (1a20a)$$

The mode precipitation fall velocity $U_{\text{f\_mode}}$ is described by a similar function, based on the mode frequency f_{mode} of the measured Doppler power density spectrum.

$$U_{\text{f\_mode}} = \frac{f_{\text{mode}}\lambda}{2}, \qquad (1b20b)$$

For each 30-minute event, the mean and mode event fall velocity correspond to the average of all minutely mean and mode values, respectively. The transfer functions presented in this work were derived using both forms of event fall velocity and assessed in terms of the RMSE and bias error (BE) of adjusted measurements relative to the DFAR. The specific fall velocity indicated for each transfer function corresponds to that which produced the lowest RMSE and BE. The POSS also provides a minutely precipitation type output corresponding to very light, light, moderate, and heavy precipitation for rain, snow, hail, and undefined precipitation. Each event is classified as ‘rain’ or ‘snow’, corresponding to a minimum 70 % occurrence of that precipitation type over the event period (i.e. at least 21 minutes of precipitation occurrence). ‘Mixed’ precipitation events correspond to the presence of both ‘rain’ and ‘snow’ for the remaining events not classified as rain or snow. ‘Undefined’ precipitation corresponds to events where the precipitation is not captured by the three other classifications.

42.4 Transfer functions with wind speed and temperature

Due to the systematic error associated with gauge undercatch, the unshielded gauge can capture less precipitation than the true amount falling in the air. The measured collection efficiency CE_{m} is defined as the ratio of the precipitation accumulation reported by the unshielded gauge P_{un} relative to that reported by the DFAR P_{DFAR} for each event, and is given by:

$$CE_{\mathrm{m}} = \frac{P_{\mathrm{un}}}{P_{\mathrm{DFAR}}}, \quad (2\underline{21})$$

Assuming that the gauge measurement uncertainties are independent and random with equivalent accumulations (corresponding to a collection efficiency equal to 1) and uncertainties, the uncertainty in the collection efficiency σ_{CE} scales with the relative magnitude of the gauge uncertainty σ_P and the event accumulation value P by error propagation.

$$\sigma_{CE} = \frac{\sqrt{2}\sigma_P}{P}, \quad (3\underline{22})$$

Collection efficiency transfer functions CE attempt to capture the performance of the unshielded gauge relative to the reference configuration based on wind speed, temperature, or other meteorological parameters. They can then be applied to adjust precipitation accumulations from an unshielded gauge in operational settings where reference measurements are not available.

$$P_{\mathrm{adj}} = \frac{P_{\mathrm{un}}}{CE}, \quad (4\underline{23})$$

~~Building upon previous work on transfer functions (Goodison, 1978;Goodison et al., 1998;Wolff et al., 2015),~~ Kochendorfer et al. (2017a;2018) used SPICE measurement data from eight test sites to develop an exponential and trigonometric transfer function based on wind speed U_{w} and air temperature T. This is referred to as $\mathrm{K_{Universal}}$ in this work (Eq. ~~5a~~24a). For wind speeds above a threshold value U_{wt} of 7.2 m s^{-1}, the wind speed is fixed at the threshold value (Eq. ~~5b~~24b) to avoid the potential for erroneous catch efficiency values at higher wind speeds that were not well represented in the SPICE measurement dataset. Based on a similar rationale, no adjustment is applied for temperatures above 5 °C. Note that while Kochendorfer et al. (2017b) considered wind speeds at both gauge height and at 10 m, U_{w} will denote the gauge height wind speed in this work.

$$CE_{\mathrm{K}}\left(U_{\mathrm{w}} \le U_{\mathrm{wt}}, T\right) = \exp\left[-b_1 U_{\mathrm{w}}\left(1 - \tan^{-1}\left(b_2 T\right) + b_3\right)\right], \quad (~~5a~~24a)$$

$$CE_{\mathrm{K}}\left(U_{\mathrm{w}} > U_{\mathrm{wt}}, T\right) = \exp\left[-b_1 U_{\mathrm{wt}}\left(1 - \tan^{-1}\left(b_2 T\right) + b_3\right)\right], \quad (~~5b~~24b)$$

The coefficients for $\mathrm{K_{Universal}}$ are provided in Table ~~1~~6.

Table ~~1~~6. Unshielded Geonor T-200B3 precipitation gauge collection efficiency transfer function coefficients for solid and mixed precipitation with 30-minute scalar mean wind speed ~~*u*~~U_{w} at gauge height for: $\mathrm{K_{Universal}}$ function with wind speed and air temperature T dependence, with constant value above wind speed threshold with Kochendorfer et al. (2017a) coefficients; $\mathrm{K_{CARE}}$ function with wind speed and air temperature dependence, with constant value above wind speed threshold; ~~present study CFD model with dependence on wind speed and mode hydrometeor fall velocity $U_{\mathrm{f\_mode}}$;~~ HE1 model with dependence on wind speed and mean hydrometeor fall velocity $U_{\mathrm{f\_mean}}$ threshold; and HE2 model with wind speed and mode hydrometeor fall velocity dependence and mode hydrometeor fall velocity threshold.

Description	Eq.	Function	Coefficients b_1	b_2	b_3	b_4	Threshold
$\mathrm{K_{Universal}}$	5	$f(U_{\mathrm{w}}, T)$	0.0785	0.729	0.407	-	U_{wt} = 7.2 m s^{-1}, $T \le 5$ °C
$\mathrm{K_{CARE}}$	5	$f(U_{\mathrm{w}}, T)$	0.1651	0.186	-0.757		U_{wt} = 7.2 m s^{-1}, $T \le 1.33$ °C

Formatted Table

~~CFD~~	~~6~~	~~$f(uU_w, uU_{f\_mode})$~~	~~0.908~~	~~1.387~~	~~0.143~~	~~2.422~~	~~$uU_w \le uU_{wc}$, $uU_w \le 10$ m s^{-1}~~
HE1	7	$f(uU_w, uU_{f\_mean})$	0.139	-	-	-	~~$uU_{f\_mean} \le 1.93$ m s^{-1}, $uU_w \le 7.19$~~5.75 m s^{-1}
HE2	8	$f(uU_w, uU_{f\_mode})$	0.244	0.0869	-	-	~~$uU_{f\_mode} \le 2.81$ m s^{-1}, $uU_w \le 0.8/(b_1-b_2uU_f)$~~

Using the same formulation, a site-specific transfer function based on wind speed and temperature was derived using the CARE dataset, for comparison with $K_{Universal}$. Best-fit regression coefficients were determined by varying the temperature threshold below 5 °C with the collection efficiency constrained to 1 above the threshold value. Solving Eq. ~~5a~~ 24a for the temperature when the collection efficiency equals 1 provides additional constraint on the b_3 coefficient as a function of the b_2 coefficient and temperature threshold T_t.

$$b_3 = \tan^{-1}(b_2 T_t) - 1, \quad (~~5c~~24c)$$

The coefficients for the CARE site-specific transfer function, referred to as K_{CARE} in this work, are provided in Table ~~4~~6. The temperature threshold was varied over the measurement range in 0.01 °C increments to provide the lowest overall RMSE. ~~The transfer function derived from CFD simulations in Part I was formulated using the wind speed and hydrometeor fall velocity u_f. The CFD model was based on time-averaged Navier-Stokes simulations with a k-ε turbulence model for 0 to 10 m s^{-1} wind speeds and Lagrangian analysis of hydrometeor trajectories for hydrometeor fall velocities between 0.5 m s^{-1} to 10 m s^{-1} representing dry snow, wet snow, and rain using a spherical drag model. The collection efficiency decreases nonlinearly with increasing wind speed, but increases with increasing u_f (Eq. 6a). A wind speed cut-off value u_{wc}, which is a function of u_f, defines the wind speed above which the CE is zero (Eq. 6b). This was derived from Eq. (6a) by solving for the lower root where the collection efficiency is zero using the quadratic formula. For wind speeds above the cut-off value, the collection efficiency is equal to 0 (Eq. 6c). These expressions were derived using CFD analysis for wind speeds up to 10 m s^{-1}. The hydrometeor fall velocity is given by the mode of the POSS Doppler velocity spectrum.~~

~~$$CE_{CFD}(u_w \le u_{wc}, u_f) = 1 - b_1 \exp(-b_2 u_f) u_w + b_3 \exp(-b_4 u_f) u_w^2, \quad (6a)$$~~

~~$$u_{wc} = \frac{b_1}{2b_3} \exp\left[(b_4 - b_2)u_f\right] - \frac{\sqrt{b_1^2 \exp(-2b_2 u_f) - 4b_3 \exp(-b_4 u_f)}}{2b_3 \exp(-b_4 u_f)}, \quad (6b)$$~~

~~$$CE_{CFD}(u_w > u_{wc}, u_f) = 0, \quad (6c)$$~~

~~5~~3 Experimental ~~R~~results

~~5~~3.1 Precipitation type

Using the minutely POSS precipitation type output, events were classified as ‘rain’, ‘snow’, ‘mixed’, or ‘undefined’ following the methodology in Sect. ~~2~~4.3. The relative occurrence of different precipitation types as reported by the POSS for the event

dataset is summarized in Table ~~2~~7. The f~~F~~all velocities in Table 7 were estimated by the POSS following the methodology in Sect. 4.3; the ~~and~~ temperatures were estimated from a YSI44212 thermistor in an aspirated Stevenson screen as described in Sect. 4.1.

Table ~~2~~7. Mean fall velocities and temperatures of precipitation events by type classification.

Precipitation phase	Fall velocities ($m\ s^{-1}$)	Temperatures (°C)	Events (#)
Snow	0.93 to 2.32	< 0.5	233
Mixed	1.2 to 4.6	-7.0 to 2.1	45
Undefined	1.0 to 4.3	-5.4 to 6.6	40
Rain	1.4 to 6.4	-4.8 to 18.9	196

Based on the mean fall velocities and temperatures for each precipitation event (Fig. 11, Table ~~2~~7), snow events occurred at temperatures below 0.5 °C and with fall velocities of 0.93 m s^{-1} to 2.32 m s^{-1}. Mixed events were characterized by mean temperatures between -7.0 °C and 2.1 °C and mean fall velocities between 1.2 m s^{-1} and 4.6 m s^{-1}, while undefined precipitation events occurred at mean temperatures between -5.4 °C and 6.6 °C and fall velocities between 1.0 m s^{-1} and 4.3 m s^{-1}. Rain events were characterized by mean temperatures between -4.8 °C and 18.9 °C and mean fall velocities between 1.4 m s^{-1} and 6.4 m s^{-1}. Over the temperature range between -5 °C and 2 °C, rain, snow, mixed, and undefined precipitation types were all present, demonstrating the challenge of estimating precipitation type using temperature alone (e.g. as done for the $K_{Universal}$ and K_{CARE} transfer functions). Within this temperature range, a wide variety of mean fall velocities, between 1 and 6 m s^{-1}, is also apparent.

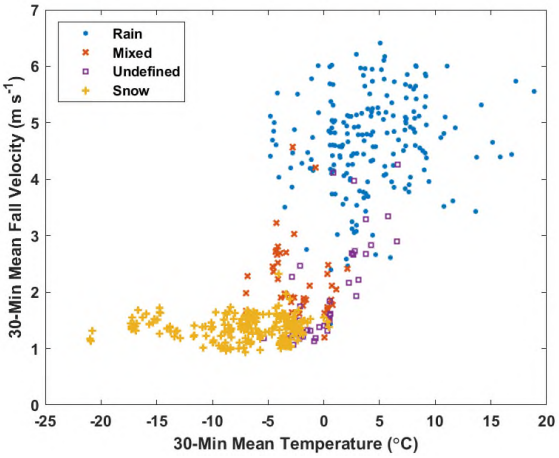

Figure 11. Mean air temperature and fall velocity for 30-minute events with rain, snow, mixed, and undefined precipitation (see Table ~~1~~ 7 for summary).

~~5~~3.2 Collection efficiency

The unshielded gauge collection efficiency results are shown as a function of the 30-minute DFAR event accumulations in Fig. 12a and stratified by precipitation type classification. The collection efficiency for rain shows less scatter and less uncertainty for higher reference precipitation accumulations. The dashed lines in Fig. 12a show the decrease in the collection efficiency uncertainty with increasing precipitation accumulation for a collection efficiency equal to 1 and a precipitation accumulation uncertainty of 0.1 mm (k = 2) given by Eq. ~~3~~22. These lines appear to capture the overall trend observed for rain events. The snowfall events show a markedly different trend, however, with collection efficiencies as low as 0.3.

The collection efficiency for all events as a function of mean wind speed and precipitation type classification is shown in Fig. 12b. For rain events, the collection efficiencies are close to 1. For snow, an approximately linear decrease in the collection efficiency with mean wind speed is apparent, with the collection efficiency decreasing to 0.3 at a wind speed of 5 m s^{-1}. Mixed precipitation collection efficiencies span a range of values between those of rain and snow. For undefined precipitation, some events have collection efficiencies close to 1 at high wind speeds, similar to rain events, while others appear to decrease with increasing wind speed in a similar fashion to that observed for snow events.

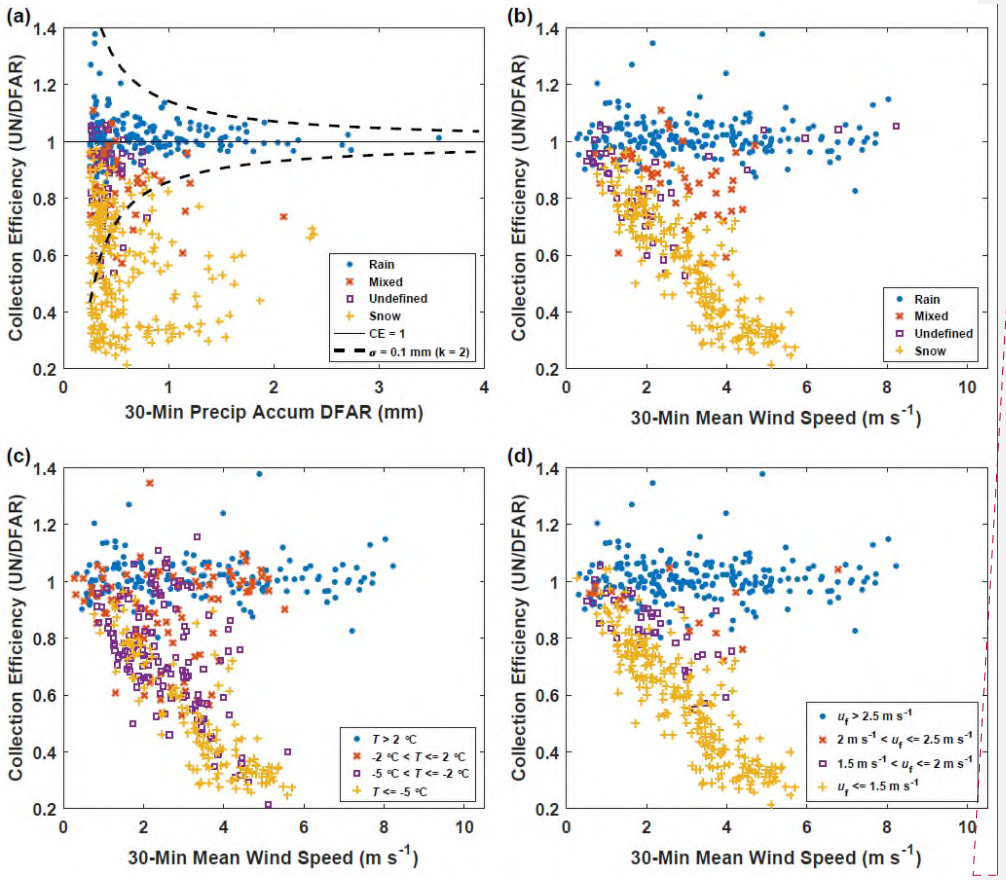

Commented [JH13]: Replaced

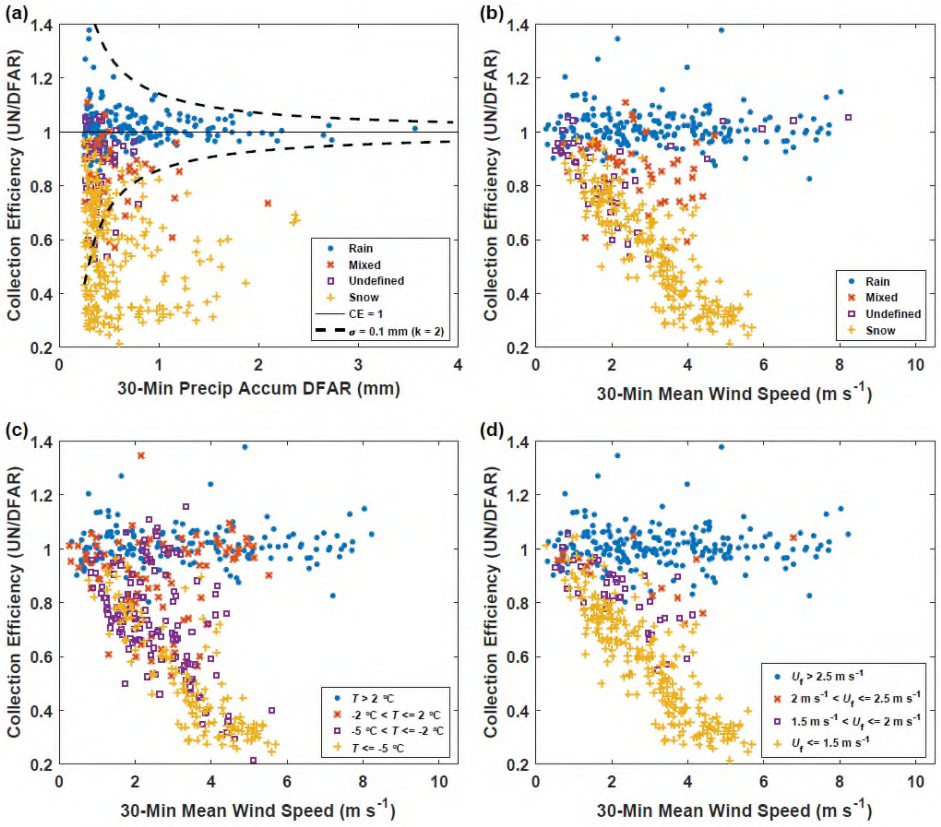

Figure 12. Collection efficiency of the unshielded gauge as a function of: (a) precipitation accumulation and event precipitation type (dashed lines illustrate accumulation uncertainty threshold); (b) wind speed and event precipitation type; (c) wind speed and mean air temperature *T* categories; and (d) wind speed and mode fall velocity ~~*U*~~$_{Pf}$ categories.

The dependence of collection efficiencies on the mean wind speed over four separate mean temperature ranges is shown in Fig. 12c. For mean event temperatures above 2 °C, the collection efficiencies are generally close to 1, typical of rain. For temperatures between -5 °C and -2 °C and between -2 °C and 2 °C, a range of collection efficiency values are observed, from those typical of snow to those typical of rain. This variation is attributed to the wide range of fall velocities within this temperature range, which includes snow, rain, and mixed precipitation events (Fig. 12b). At colder temperatures, below -5 °C,

collection efficiencies appear to decrease approximately linearly with wind speed, consistent with the trend observed for snow events in Fig. 12b.

Stratifying the collection efficiency results as a function of mean event wind speed by the mode fall velocity shows more distinct trends (Fig. 12d) relative to those observed when stratifying by temperature (Fig. 12c). Collection efficiencies are close to 1 for fall velocities greater than 2.5 m s^{-1}, generally corresponding to rain. Conversely, fall velocities below 1.5 m s^{-1} show an approximately linear decrease in collection efficiency with increasing wind speed up to about 6 m s^{-1}. A number of the values with higher collection efficiencies in this low fall velocity range correspond to mixed precipitation, where both snow and rain may be present. Between 1.5 m s^{-1} to 2.5 m s^{-1} fall velocity, intermediate collection efficiency values are evident, with collection efficiencies transitioning from lower to higher values, despite a fewer number of observations in this range.

~~The dependence of the collection efficiency on 30-minute mean air temperature and the 30-minute mean of mode fall velocity values for 2 m s^{-1} to 4 m s^{-1} wind speeds is shown in Figs. 3a and 3b, respectively. This range of wind speeds shows the most significant overlap among rain, snow, mixed and undefined precipitation, and is sufficiently high that a wide range of collection efficiencies is observed. The collection efficiency generally increases with temperature (Fig. 3a), although values are spread broadly across air temperature values, with collection efficiencies below 0.6 occurring between -22 °C and 0 °C. More clearly-defined trends with fall velocity are apparent, with collection efficiencies increasing sharply with fall velocity up to ~ 2.5 m s^{-1} and distributed around 1 for higher fall velocities.~~

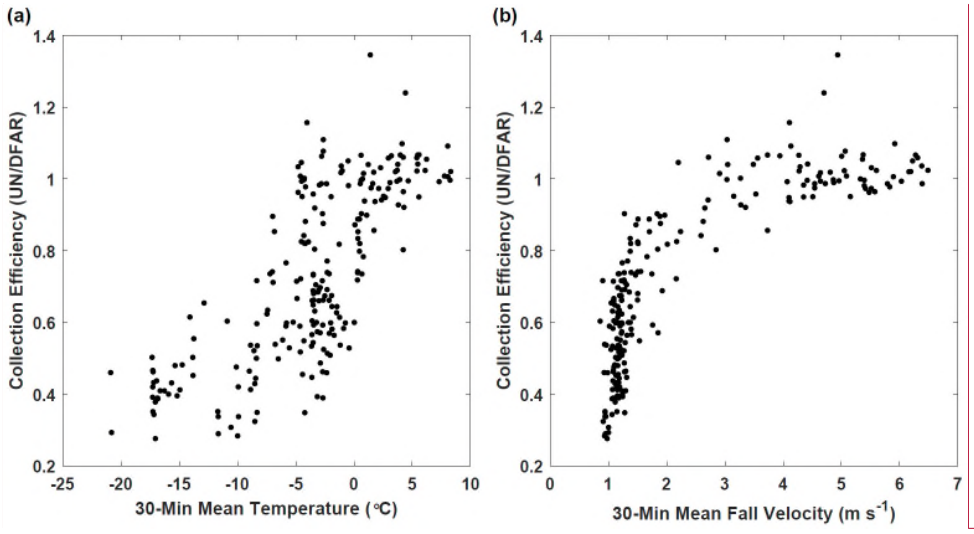

Commented [JH14]: Removed

~~**Figure 3.** Collection efficiency of unshielded gauge for 2 m s^{-1} to 4 m s^{-1} 30-minute mean wind speeds with (a) 30-minute mean air temperature and (b) 30-minute mean of mode fall velocities.~~

5~~3~~.3 Derivation of fall velocity transfer functions from CE results

Two additional transfer functions were formulated based on the apparent linear dependence of CE on wind speed for different hydrometeor fall velocity regimes observed in experimental results (Fig. 12d). These functions are applicable to all hydrometeor types, and have different fall velocity thresholds to describe the transition of precipitation phase from the lower fall velocities characteristic of snow to the higher fall velocities characteristic of rain and mixed precipitation.

The first transfer function, referred to as HE1, is based on the assumption of a linear decrease in collection efficiency CE_{HE1} with wind speed U_{w} for hydrometeors with mean fall velocity U_{f} below 1.93 m s^{-1}, generally corresponding to snowfall. This linear decrease is extrapolated up to a ~~7.19~~5.75 m s^{-1} wind speed threshold (Eq. ~~7a~~25a), above which the collection efficiency for snowfall is ~~zero~~ 0.2 (Eq. ~~7b~~25b), following the general approach of Kochendorfer et al. (2017a). For hydrometeors with mean fall velocity greater than 1.93 m s^{-1}, corresponding to mixed and liquid precipitation, the collection efficiency is 1 (Eq. ~~7c~~25c). The fall velocity threshold was varied over the measurement fall velocity range in 0.01 m s^{-1} increments, with the threshold of 1.93 m s^{-1} found to provide the lowest overall RMSE.

~~$CE_{HE1}\left(u_{\mathrm{w}} \le 7.19\,\mathrm{m\,s^{-1}}, u_{\mathrm{f}} \le 1.93\,\mathrm{m\,s^{-1}}\right) = 1 - b_1 u_{\mathrm{w}}$~~ $CE_{\mathrm{HE1}}\left(U_{\mathrm{w}} \le 5.75\,\mathrm{m\,s^{-1}}, U_{\mathrm{f}} \le 1.93\,\mathrm{m\,s^{-1}}\right) = 1 - b_1 U_{\mathrm{w}}$, (~~7a~~25a)

~~$CE_{\mathrm{HE1}}\left(u_{\mathrm{w}} > 7.19\,\mathrm{m\,s^{-1}}, u_{\mathrm{f}} \le 1.93\,\mathrm{m\,s^{-1}}\right) = 0$~~ $CE_{\mathrm{HE1}}\left(U_{\mathrm{w}} > 5.75\,\mathrm{m\,s^{-1}}, U_{\mathrm{f}} \le 1.93\,\mathrm{m\,s^{-1}}\right) = 0.2$, (~~7b~~25b)

$CE_{\mathrm{HE1}}\left(U_{\mathrm{f}} > 1.93\,\mathrm{m\,s^{-1}}\right) = 1$, (~~7c~~25c)

The second transfer function, referred to as HE2, adds another dimension to describe the slope of the linear decrease in CE with increasing wind speed: the hydrometeor fall velocity. For mode fall velocity U_{f} below 2.81 m s^{-1} and wind speed U_{w} below the ~~cut-off~~threshold value, which is also dependent on the fall velocity, the collection efficiency CE_{HE2} is assumed to decrease linearly with decreasing wind speed for a given hydrometeor fall velocity~~to zero~~ (Eq. ~~8a~~26a). For mode fall velocity below 2.81 m s^{-1} and wind speed above the ~~cut-off~~threshold value, the collection efficiency is ~~zero~~ 0.2 (Eq. ~~8b~~26b). For mode fall velocity above 2.81 m s^{-1}, the collection efficiency is equal to 1 (Eq. ~~8c~~26c). The fall velocity threshold was varied over the measurement fall velocity range in 0.01 m s^{-1} increments with the threshold of 2.81 m s^{-1} found to provide the lowest overall RMSE.

~~$CE_{\mathrm{HE2}}\left(u_{\mathrm{w}} \le \frac{1}{b_1 - b_2 u_{\mathrm{f}}}, u_{\mathrm{f}} \le 2.81\,\mathrm{m\,s^{-1}}\right) = 1 - \left(b_1 - b_2 u_{\mathrm{f}}\right) u_{\mathrm{w}}$~~ $CE_{\mathrm{HE2}}\left(U_{\mathrm{w}} \le \frac{0.8}{b_1 - b_2 U_{\mathrm{f}}}, U_{\mathrm{f}} \le 2.81\,\mathrm{m\,s^{-1}}\right) = 1 - \left(b_1 - b_2 U_{\mathrm{f}}\right) U_{\mathrm{w}}$

, (~~8a~~26a)

~~$CE_{\mathrm{HE2}}\left(u_{\mathrm{w}} > \frac{1}{b_1 - b_2 u_{\mathrm{f}}}, u_{\mathrm{f}} \le 2.81\,\mathrm{m\,s^{-1}}\right) = 0$~~ $CE_{\mathrm{HE2}}\left(U_{\mathrm{w}} > \frac{0.8}{b_1 - b_2 U_{\mathrm{f}}}, U_{\mathrm{f}} \le 2.81\,\mathrm{m\,s^{-1}}\right) = 0.2$, (~~8b~~26b)

$$CE_{\mathrm{HE2}}\left(U_{\mathrm{f}} > 2.81\mathrm{m\ s^{-1}}\right) = 1, \quad (8c26c)$$

53.4 Assessment of transfer functions: collection efficiency

Observed collection efficiencies were compared with adjusted values using both existing transfer functions from SPICE and those presented in this work. Results are presented in Fig. 413, with relevant transfer function parameters compiled in Tables 15 and 6, and resulting bias errors, root mean square errors, and correlation coefficients (r) presented in Table 38. To further contextualize the assessment of the different transfer functions, the RMSE results are presented for different precipitation classifications, temperature ranges, and fall velocity ranges in Tables 4 to 6 9, respectively.

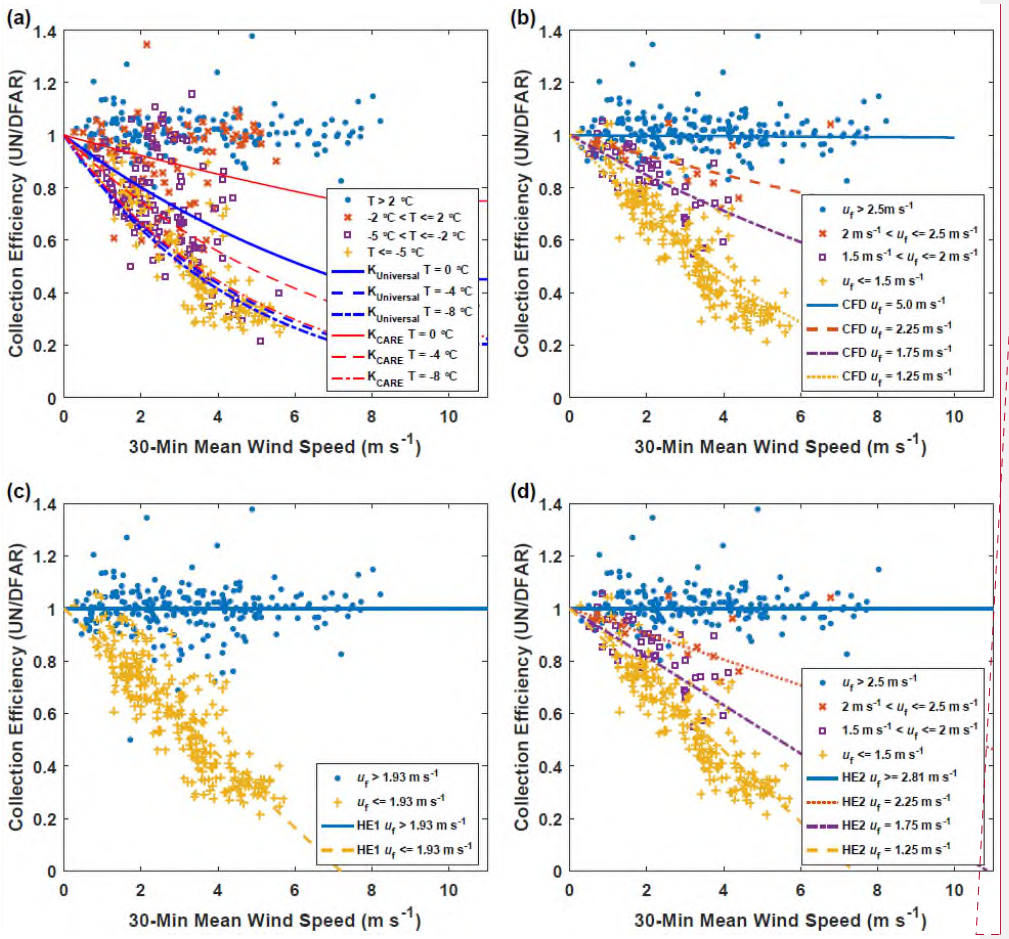

Commented [JH15]: Replaced

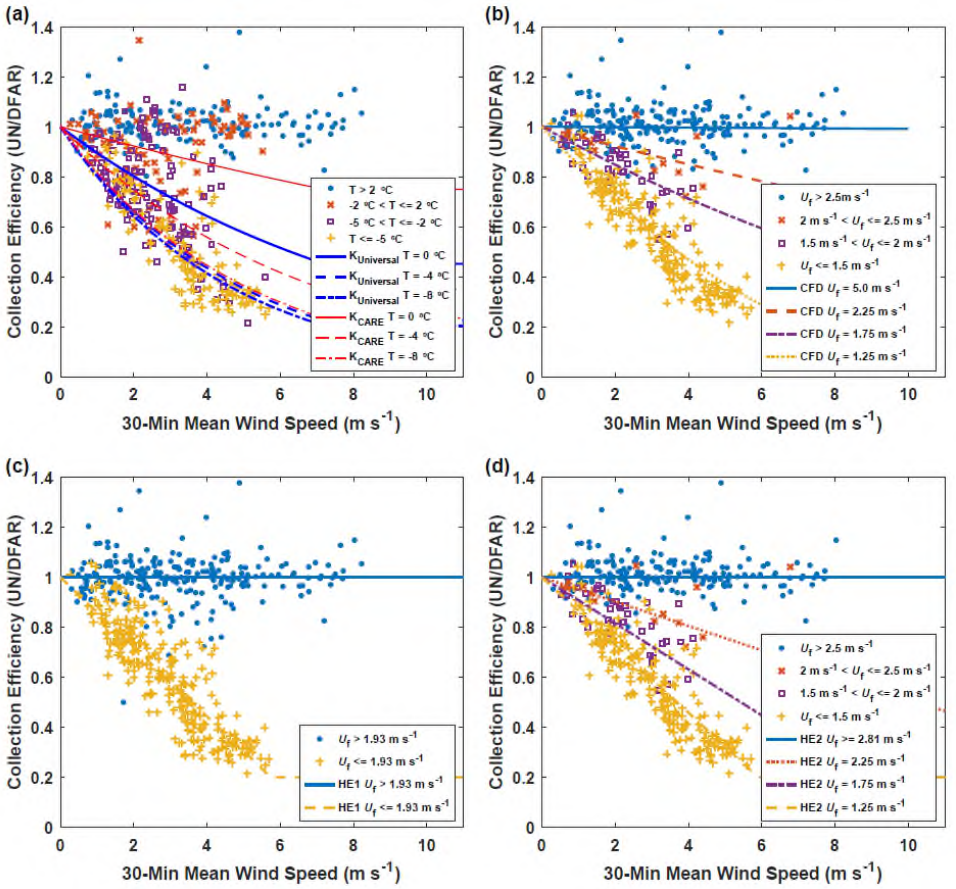

Figure 413. Collection efficiency of unshielded gauge as a function of wind speed for: (a) mean air temperature *T* categories for the $K_{Universal}$ and K_{CARE} transfer functions; (b) mode fall velocity u_{Pf} categories with the CFD transfer function; (c) mean fall velocity u_{Pf} categories for the HE1 transfer function; and (d) mode fall velocity u_{Pf} categories with the HE2 transfer function.

Table ~~3~~8. Unshielded gauge 30-minute event bias error (BE), root mean square error (RMSE), correlation coefficient (r), and number of events (N) for collection efficiency and precipitation accumulation between the unshielded and reference DFAR shielded Geonor T-200B3 gauge for: unadjusted comparison; $K_{Universal}$ transfer function with wind speed and air temperature dependence; K_{CARE} transfer function with wind speed and air temperature dependence; present study CFD transfer function with wind speed and mode fall velocity dependence; HE1 transfer function with wind speed and mean fall velocity dependence; and HE2 transfer function with wind speed and mode fall velocity dependence. Statistics are based on the comparison of experimental results from the CARE site between November 1 and April 30, 2013/14 and 2014/15.

	Collection efficiency			Precip accum (mm)			
Description	BE	RMSE	r	BE	RMSE	r	N
Unadjusted	-	-	-	-0.13	0.24	0.900	514
$K_{Universal}$	0.07	0.15	0.853	0.07	0.20	0.949	514
K_{CARE}	-0.005	0.12	0.878	0.002	0.13	0.963	514
CFD	-0.02	0.08	0.949	0.011	0.08	0.986	514
HE1	0.0004	0.10	0.928	0.006	0.09	0.983	514
HE2	-0.009	0.08	0.950	0.006	0.07	0.988	514

Table ~~4~~9. Unshielded gauge 30-minute event collection efficiency RMSE results stratified by: ~~between the unshielded and reference DFAR shielded Geonor T-200B3 gauge by~~(a) POSS precipitation type; (b) temperature; and (c) fall velocity.~~ for:~~ Results are shown for: $K_{Universal}$ transfer function with wind speed and air temperature dependence; K_{CARE} transfer function with wind speed and air temperature dependence; present study CFD transfer function with wind speed and mode fall velocity dependence; HE1 transfer function with wind speed and mean fall velocity dependence; and HE2 transfer function with wind speed and mode fall velocity dependence. Statistics are based on the comparison of experimental results from the CARE site between November 1 and April 30, 2013/14 and 2014/15.

			RMSE	
(a) Description	Rain (N = 196)	Mixed (N = 45)	Undefined (N = 40)	Snow (N = 233)
$K_{Universal}$	0.17	0.27	0.09	0.09
K_{CARE}	0.12	0.20	0.13	0.11
CFD	0.08	0.09	0.09	0.09
HE1	0.07	0.16	0.08	0.10
HE2	0.08	0.10	0.09	0.08
(b) Description	$T > 2$ °C (N = 150)	-2 °C < $T \leq$ 2 °C (N = 89)	-5 °C < $T \leq$ -2 °C (N = 134)	$T \leq$ -5 °C (N = 141)
$K_{Universal}$	0.08	0.19	0.21	0.11
K_{CARE}	0.07	0.13	0.17	0.10
CFD	0.09	0.08	0.08	0.09
HE1	0.07	0.10	0.11	0.10
HE2	0.09	0.08	0.07	0.08
(c) Description	~~u~~$U_f > 2.5$ m s^{-1} (N = 212)	2 m s^{-1} < ~~U~~$U_f \leq 2.5$ m s^{-1} (N = 15)	1.5 m s^{-1} < ~~u~~$U_f \leq 2$ m s^{-1} (N = 40)	~~u~~$U_f \leq 1.5$ m s^{-1} (N = 247)
$K_{Universal}$	0.19	0.23	0.16	0.09
K_{CARE}	0.13	0.17	0.12	0.11
CFD	0.08	0.10	0.08	0.09
HE1	0.08	0.13	0.15	0.10
HE2	0.08	0.12	0.08	0.08

	RMSE			
Description	Rain (N = 196)	Mixed (N = 45)	Undefined (N = 40)	Snow (N = 233)
$K_{Universal}$	0.17	0.27	0.09	0.09
K_{CARE}	0.12	0.20	0.13	0.11
CFD	0.08	0.09	0.09	0.09
HE1	0.07	0.16	0.08	0.10
HE2	0.08	0.10	0.09	0.08

Table 5. Unshielded gauge 30-minute event collection efficiency RMSE between the unshielded and reference DFAR shielded Geonor T-200B3 gauge by temperature classification for: $K_{Universal}$ transfer function with wind speed and air temperature dependence; K_{CARE} transfer function with wind speed and air temperature dependence; present study CFD transfer function with wind speed and mode fall velocity dependence; HE1 transfer function with wind speed and mean fall velocity dependence; and HE2 transfer function with wind speed and mode fall velocity dependence. Statistics are based on the comparison of experimental results from the CARE site between November 1 and April 30, 2013/14 and 2014/15.

	RMSE			
Description	$T > 2$ °C (N = 150)	-2 °C $< T \leq 2$ °C (N = 89)	-5 °C $< T \leq -2$ °C (N = 134)	$T \leq -5$ °C (N = 141)
$K_{Universal}$	0.08	0.19	0.21	0.11
K_{CARE}	0.07	0.13	0.17	0.10
CFD	0.09	0.08	0.08	0.09
HE1	0.07	0.10	0.11	0.10
HE2	0.09	0.08	0.07	0.08

Table 6. Unshielded gauge 30-minute event collection efficiency RMSE between the unshielded and reference DFAR shielded Geonor T-200B3 gauge by fall velocity classification for: $K_{Universal}$ transfer function with wind speed and air temperature dependence; K_{CARE} transfer function with wind speed and air temperature dependence; present study CFD transfer function with wind speed and mode fall velocity dependence; HE1 transfer function with wind speed and mean fall velocity dependence; and HE2 transfer function with wind speed and mode fall velocity dependence. Statistics are based on the comparison of experimental results from the CARE site between November 1 and April 30, 2013/14 and 2014/15.

	RMSE			
Description	$u_{Uf} > 2.5$ m s^{-1} (N = 212)	2 m s$^{-1} < u_{Uf} \leq 2.5$ m s^{-1} (N = 15)	1.5 m s$^{-1} < u_{Uf} \leq 2$ m s^{-1} (N = 40)	$u_{Uf} \leq 1.5$ m s^{-1} (N = 247)
$K_{Universal}$	0.19	0.23	0.16	0.09
K_{CARE}	0.13	0.17	0.12	0.11
CFD	0.08	0.10	0.08	0.09
HE1	0.08	0.13	0.15	0.10
HE2	0.08	0.12	0.08	0.08

Both $K_{Universal}$ and the site climate-specific K_{CARE} transfer function have continuous temperature dependence and display similar profiles at -8 °C, with the collection efficiency for the K_{CARE} transfer function decreasing more gradually with wind speed

compared to the $K_{Universal}$ transfer function at -4 °C and 0 °C (Fig. ~~4a~~13a). Using the approach outlined in Sect. ~~2~~4.4, a temperature ~~cutoff~~ threshold T_t of 1.33 °C for the best-fit K_{CARE} transfer function was found to minimize the precipitation accumulation RMSE. The overall collection efficiency root mean square error is reduced from 0.15 for the $K_{Universal}$ transfer function to 0.12 for the K_{CARE} transfer function (Table ~~3~~8). The bias error is also reduced from 0.07 for the $K_{Universal}$ transfer function to -0.005 for the best-fit K_{CARE} transfer function. For $K_{Universal}$ and K_{CARE}, respectively, the RMSE is reduced from 0.17 to 0.12 for rain and from 0.27 to 0.20 for mixed precipitation, with slightly elevated RMSE from 0.09 to 0.13 for undefined precipitation and 0.09 to 0.11 for snow (Table ~~4~~9a). For mean event temperatures between -2 °C and 2 °C, and between -5 °C and -2 °C, respectively, the RMSE values of 0.19 and 0.21 for the $K_{Universal}$ transfer function are relatively large compared to the 0.13 and 0.17 values for the K_{CARE} transfer function (Table ~~5~~9b). This results from the more gradual decrease in the K_{CARE} transfer function with wind speed over these temperature ranges (Fig. ~~4a~~13a).

A comparison of the CFD transfer function with observed CE is shown in Fig. ~~4b~~13b. Overall, the measured data have less scatter when stratified by fall velocity than when stratified by temperature (Table ~~3~~8, Figs. ~~4a~~ 13a and b). The CFD transfer function provides a lower overall RMSE (0.08) and higher r (0.949) relative to the $K_{Universal}$ and K_{CARE} transfer functions based on temperature. Reductions in the collection efficiency RMSE using the CFD transfer function are most pronounced for rain and mixed precipitation (Table ~~4~~9a) and for mean event temperatures between -2 °C and 2 °C and between -5 °C and -2 °C (Table ~~5~~9b) compared with the $K_{Universal}$ and K_{CARE} functions. Collection efficiency RMSE values are between 0.08 and 0.10 over all fall velocity classes, despite fewer numbers of events with fall velocities between 1.5 m s^{-1} and 2.5 m s^{-1} (Table ~~6~~9c).

The HE1 transfer function provides good agreement with observed data in the mean fall velocity regimes relevant to snow and rain (Fig. ~~4c~~13c), resulting in an overall RMSE of 0.10, BE of 0.0004, and r of 0.928 (Table ~~3~~8). The RMSE for mixed precipitation is 0.16, which is lower than that of the K_{CARE} transfer function with temperature (0.20) but higher that that of the CFD model (0.09), which varies continuously with fall velocity (Table ~~4~~9a).

The HE2 function better captures the observed collection efficiencies for mode fall velocities between the snow and rain regimes (Fig. ~~4d~~13d), improving the overall RMSE to 0.08 and r to 0.95, while increasing slightly the BE (-0.009) relative to HE1 (Table ~~3~~8). Note the distinction between mean fall velocity for HE1 and mode fall velocity for HE2 (and CFD). In general, the Doppler frequency spectrum tends to be skewed such that mode fall velocities are slightly lower than the mean fall velocities, impacting the fits to observed data. The HE2 transfer function provides similar results to that of the CFD transfer function, with slightly higher RMSE values for mixed precipitation and slightly reduced RMSE values for snow (Table ~~4~~9a) and temperatures below -2 °C (Table ~~5~~9b). For intermediate fall velocities between 2.0 m s^{-1} and 2.5 m s^{-1}, the HE2 transfer function, with a linear change in collection efficiency with fall velocity, has a higher RMSE (0.12) than that for the CFD function (0.10), which exhibits a nonlinear change in collection efficiency with fall velocity (Table ~~6~~9c). Only 15 events were recorded in this intermediate fall velocity range with higher uncertainty relative to the CFD function. In contrast, 212 events were recorded at fall velocities above 2.5 m s^{-1} and 247 events at fall velocities below 1.5 m s^{-1}, representing a greater proportion of the events with lower RMSE relative to the CFD function.

53.5 Assessment of transfer functions: precipitation accumulation

The unadjusted and adjusted accumulated precipitation values are compared with reference DFAR accumulation measurements in Fig. 514. Bias, RMSE, and correlation coefficient results are shown in Table 38. Similar to the approach for assessing transfer functions based on collection efficiency results in Sect. 53.4, the precipitation accumulation RMSE results for each transfer function are assessed by precipitation classification, temperature range, and fall velocity range in Table 10~~s 7 to 9, respectively~~.

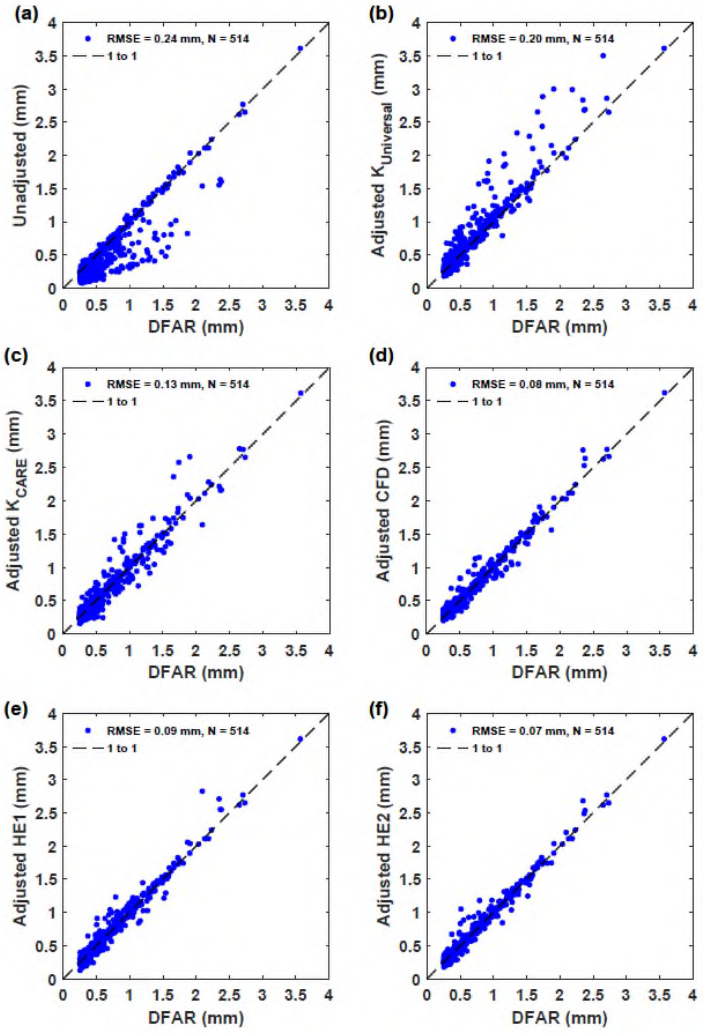

Figure 514. Unshielded and reference DFAR 30-minute event precipitation accumulation comparison for: (a) unadjusted precipitation accumulation; (b) $K_{Universal}$ continuous transfer function with wind speed and air temperature dependence; (c) K_{CARE} continuous transfer function with wind speed and air temperature dependence; (d) CFD transfer function with wind speed and fall velocity dependence; (e) HE1 transfer function with wind speed and fall velocity dependence; and (f) HE2 transfer function with wind speed and fall velocity dependence.

Table ~~7~~10. Unshielded gauge 30-minute event RMSE (mm) results stratified by: (a) POSS precipitation type; (b) temperature; and (c) fall velocity. Results are shown for~~between the unshielded and reference DFAR shielded Geonor T-200B3 gauge by POSS precipitation type for~~: unadjusted comparison; $K_{Universal}$ transfer function with wind speed and air temperature dependence; K_{CARE} transfer function with wind speed and air temperature dependence; present study CFD transfer function with wind speed and mode fall velocity dependence; HE1 transfer function with wind speed and mean fall velocity dependence; and HE2 transfer function with wind speed and mode fall velocity dependence. Statistics are based on the comparison of experimental results from the CARE site between November 1 and April 30, 2013/14 and 2014/15.

	RMSE (mm)			
(a) Description	Rain (N = 196)	Mixed (N = 45)	Undefined (N = 40)	Snow (N = 233)
Unadjusted	0.04	0.15	0.09	0.35
$K_{Universal}$	0.25	0.33	0.05	0.10
K_{CARE}	0.14	0.22	0.06	0.11
CFD	0.04	0.07	0.04	0.11
HE1	0.04	0.17	0.04	0.10
HE2	0.04	0.09	0.04	0.09
(b) Description	T > 2 °C (N = 150)	-2 °C < T ≤ 2 °C (N = 89)	-5 °C < T ≤ -2 °C (N = 134)	T ≤ -5 °C (N = 141)
Unadjusted	0.04	0.14	0.23	0.39
$K_{Universal}$	0.05	0.25	0.29	0.12
K_{CARE}	0.04	0.11	0.20	0.12
CFD	0.05	0.06	0.08	0.11
HE1	0.04	0.12	0.09	0.10
HE2	0.05	0.07	0.08	0.09
(c) Description	~~u~~U_f > 2.5 m s^{-1} (N = 212)	2 m s^{-1} < ~~u~~U_f ≤ 2.5 m s^{-1} (N = 15)	1.5 m s^{-1} < ~~u~~U_f ≤ 2 m s^{-1} (N = 40)	~~u~~U_f ≤ 1.5 m s^{-1} (N = 247)
Unadjusted	0.04	0.06	0.16	0.34
$K_{Universal}$	0.26	0.22	0.22	0.10
K_{CARE}	0.15	0.14	0.15	0.11
CFD	0.04	0.05	0.06	0.10
HE1	0.04	0.06	0.16	0.10
HE2	0.04	0.06	0.07	0.09

	~~RMSE (mm)~~			
~~Description~~	~~Rain (N = 196)~~	~~Mixed (N = 45)~~	~~Undefined (N = 40)~~	~~Snow (N = 233)~~
~~Unadjusted~~	~~0.04~~	~~0.15~~	~~0.09~~	~~0.35~~
~~$K_{Universal}$~~	~~0.25~~	~~0.33~~	~~0.05~~	~~0.10~~
~~K_{CARE}~~	~~0.14~~	~~0.22~~	~~0.06~~	~~0.11~~
~~CFD~~	~~0.04~~	~~0.07~~	~~0.04~~	~~0.11~~
~~HE1~~	~~0.04~~	~~0.17~~	~~0.04~~	~~0.10~~
~~HE2~~	~~0.04~~	~~0.09~~	~~0.04~~	~~0.09~~

~~**Table 8.** Unshielded gauge 30-minute event RMSE (mm) between the unshielded and reference DFAR shielded Geonor T-200B3 gauge by temperature classification for: unadjusted comparison; $K_{Universal}$ transfer function with wind speed and air temperature dependence; K_{CARE} transfer function with wind speed and air temperature dependence; present study CFD transfer function with wind speed and mode fall~~

velocity dependence; HE1 transfer function with wind speed and mean fall velocity dependence; and HE2 transfer function with wind speed and mode fall velocity dependence. Statistics are based on the comparison of experimental results from the CARE site between November 1 and April 30, 2013/14 and 2014/15.

	RMSE (mm)			
Description	$T > 2$ °C (N = 150)	-2 °C < $T \leq$ 2 °C (N = 89)	-5 °C < $T \leq$ -2 °C (N = 134)	$T \leq$ -5 °C (N = 141)
Unadjusted	0.04	0.14	0.23	0.39
$K_{Universal}$	0.05	0.25	0.29	0.12
K_{CARE}	0.04	0.11	0.20	0.12
CFD	0.05	0.06	0.08	0.11
HE1	0.04	0.12	0.09	0.10
HE2	0.05	0.07	0.08	0.09

Table 9. Unshielded gauge 30-minute event RMSE (mm) between the unshielded and reference DFAR shielded Geonor T-200B3 gauge by fall velocity classification for: unadjusted comparison; $K_{Universal}$ transfer function with wind speed and air temperature dependence; K_{CARE} transfer function with wind speed and air temperature dependence; present study CFD transfer function with wind speed and mode fall velocity dependence; HE1 transfer function with wind speed and mean fall velocity dependence; and HE2 transfer function with wind speed and mode fall velocity dependence. Statistics are based on the comparison of experimental results from the CARE site between November 1 and April 30, 2013/14 and 2014/15.

	RMSE (mm)			
Description	$uU_f > 2.5$ m s^{-1} (N = 212)	2 m s^{-1} < $uU_f \leq 2.5$ m s^{-1} (N = 15)	1.5 m s^{-1} < $uU_f \leq 2$ m s^{-1} (N = 40)	$uU_f \leq 1.5$ m s^{-1} (N = 247)
Unadjusted	0.04	0.06	0.16	0.34
$K_{Universal}$	0.26	0.22	0.22	0.10
K_{CARE}	0.15	0.14	0.15	0.11
CFD	0.04	0.05	0.06	0.10
HE1	0.04	0.06	0.16	0.10
HE2	0.04	0.06	0.07	0.09

In the comparison of unadjusted accumulation measurements with reference values (Fig. 5a14a), some values fall along the 1-to-1 line, while others are considerably lower. The values along the 1-to-1 line generally correspond to rain events with high precipitation fall velocity, or to events with low mean wind speeds. The RMSE for the unadjusted unshielded gauge measurements relative to the DFAR is 0.24 mm, with a bias error of -0.13 mm and correlation coefficient of 0.900 (Table 38). Using the $K_{Universal}$ transfer function, with wind and temperature dependence, shifts the adjusted values up to and above the 1-to-1 line (Fig. 5b14b). This yields a positive bias error of 0.07 mm, reduced RMSE of 0.20 mm, and correlation coefficient of 0.949 (Table 38) relative to the unadjusted measurements (Fig. 5a14a). While the $K_{Universal}$ transfer function greatly reduces the RMSE for snow from 0.35 mm to 0.10 mm compared with unadjusted values, the RMSE is increased from 0.04 mm to 0.25 mm for rain, and from 0.15 mm to 0.33 mm for mixed precipitation (Table 710a). Compared with the unadjusted results, RMSE increases for the $K_{Universal}$ function are also apparent for temperatures between -2 °C and 2 °C and between -5 °C and -2 °C (Table 810b), and for fall velocities greater than 1.5 m s^{-1} (Table 910c).

Applying the site-specific K_{CARE} transfer function, based on the best-fit results to the CARE SPICE dataset, results in a reduced bias error of 0.002 mm, lower RMSE of 0.13 mm, and higher correlation coefficient of 0.963 (Table ~~3~~8) relative to the $K_{Universal}$ results, with the scatter in adjusted accumulations more evenly balanced across the 1-to-1 line (Fig. ~~5e~~14c). The scatter in adjusted values using the K_{CARE} transfer function results primarily from mixed precipitation (Table ~~7~~10a) at temperatures between -5 °C and -2 °C (Table ~~8~~10b). Compared to the $K_{Universal}$ transfer function, the K_{CARE} transfer function has lower RMSE values for rain (0.14 mm) and mixed precipitation (0.22 mm), with 0.01 mm higher RMSE for undefined precipitation and snow (Table ~~7~~10a). The more rapid increase in collection efficiency with temperature for K_{CARE} relative to $K_{Universal}$ reduces the overadjustment of some of the rain and mixed precipitation events at temperatures between -5 °C and -2 °C, at the expense of the underadjustment of some snow events in this temperature range. It is also worth noting that the adjusted precipitation accumulation RMSE for the K_{CARE} transfer function is larger than that for unadjusted results for rain and mixed precipitation, similar to the results for $K_{Universal}$. Both the $K_{Universal}$ and K_{CARE} transfer functions with temperature show signs of heteroscedasticity, with an increased spread of values with increasing magnitude of event precipitation accumulation.

Applying the CFD transfer function results in a greatly reduced spread of values about the 1-to-1 line (Fig. ~~5d~~14d). The spread does not appear to increase with increasing precipitation accumulation. The overall RMSE is reduced to 0.08 mm, 2.5 times lower than that for the $K_{Universal}$ transfer function, with a bias error of 0.011 mm and correlation coefficient of 0.986 (Table ~~3~~8). The RMSE is reduced from 0.25 mm for the $K_{Universal}$ transfer function to 0.04 mm using the CFD transfer function for rain, and from 0.33 mm to 0.07 mm (4.7 times lower) for mixed precipitation, while RMSE results for undefined precipitation and snow are within 0.01 mm (Table ~~7~~10a). Reductions in the RMSE using the CFD transfer function compared with the $K_{Universal}$ transfer function are most pronounced for mean event temperatures between -5 °C and 2 °C (Table ~~8~~10b). Over this temperature range, rain, mixed precipitation, and snow may be present, corresponding to a wide range of fall velocities and collection efficiencies. The CFD transfer function is better able to distinguish among these precipitation types – and their respective collection efficiencies – based on its dependence on hydrometeor fall velocity. Across the fall velocity classifications in Table ~~9~~10c, the RMSE using the CFD transfer function increases from 0.04 mm for fall velocities greater than 2.5 m s^{-1} to 0.10 mm for fall velocities less than 1.5 m s^{-1}. As shown in Table ~~9~~10c, the RMSE for the CFD transfer function matches the value for unadjusted measurements at fall velocities greater than 2.5 m s^{-1}, where collection efficiencies are close to 1. At lower fall velocities, where the bias due to gauge undercatch is more prevalent, the RMSE values for the CFD function are lower than those for the unadjusted measurements.

Using the HE1 transfer function results in similar overall improvement in the agreement between adjusted and DFAR accumulation values as observed for the CFD function (Fig. ~~5e~~14e). The adjusted values appear to be distributed symmetrically about the 1-to-1 line. Furthermore, there is close agreement over the full range of accumulation values; that is, the spread in values does not increase with the magnitude of precipitation accumulation. This results in a lower RMSE of 0.09 mm and a higher correlation coefficient of 0.983 relative to the K_{CARE} transfer function results. While the RMSE for rain (0.04 mm) using the HE1 transfer function is improved compared with the K_{CARE} transfer function results, the RMSE for mixed precipitation is only marginally better (0.17 mm).

Applying the HE2 transfer function provides further improvement, with adjusted accumulation values more tightly clustered around the 1-to-1 line (Fig. ~~5f~~14f). The overall RMSE is 0.07 mm, which is 3.3 times lower than that for the unadjusted unshielded gauge measurements, and 1.8 times lower than the K_{CARE} transfer function based on mean event temperature and wind speed. The HE2 transfer function exhibits the lowest overall RMSE for snow (0.09 mm), with a RMSE of 0.09 mm for mixed precipitation, which is slightly higher than that for the CFD function (0.07 mm), but much lower than that for the K_{CARE} (0.22 mm) and HE1 (0.17 mm) transfer functions. Further, the correlation coefficient of 0.988 is the highest among the transfer functions assessed.

6 Discussion

6.1 Modelling discussion

Commented [JH16]: Sect. 6.1 added from Part I

6.1.1 Numerical modelling results

The time-averaged numerical model describes the three-dimensional airflow around the unshielded Geonor gauge, including the updraft above the leading edge of the gauge orifice and downdraft at the back of the gauge orifice shown in previous studies (Thériault et al., 2012;Colli et al., 2016a;Baghapour et al., 2017). The updraft velocity increases sharply with height above the leading edge of the gauge orifice, which appears to play an important role in the horizontal spreading and capture of hydrometeors, particularly for lower fall velocity hydrometeors (Fig~~s~~. 2 and ~~3~~4). These velocities scale with the wind speed, as shown previously by Colli et al. (2016a), and the relative magnitudes of the wind speed and hydrometeor fall velocity influence the collection efficiency. The hydrometeor fall velocity influences both the free-stream approach angle of hydrometeors before they encounter the local airflow around the gauge and the degree of coupling between the hydrometeor trajectories and the local airflow. Hydrometeors with fall velocities above 2 m s^{-1} fall more vertically, and their paths shows less deviation with the updraft and local airflow around the gauge orifice (Fig. 4). Hydrometeors with lower fall velocities have a smaller approach angle and are more closely coupled to the local airflow around the gauge orifice.

The model was validated ~~with~~by comparison with existing models (Fig. 3), with differences attributed in part to differences in model geometry. ~~Normalized velocities along the gauge centerline in the present study show good agreement with the *k-w* SST simulation results of both Colli et al. (2016a) and Baghapour et al. (2017), as shown in Fig. 3.~~ Peak normalized velocities show very good agreement with Baghapour et al. (2017) k-ω SST simulation results, which used a similar refined orifice thickness as that in the present study. Reductions in the peak gauge centerline velocity relative to the results from Colli (2016b) in Fig. 3 may result from refinements in the gauge geometry used in the present study, including the orifice thickness. This reasoning is supported by Sevruk et al. (1994), who demonstrated that reductions in the orifice thickness can reduce the ~~wind speed~~ local airflow velocity over the gauge. The sensitivity of simulation results to the model geometry is discussed in greater detail by Baghapour et al. (2017) and is an area for future study.

The numerical results for this study are based on a 5 % inlet turbulence value that acts as a bulk turbulence in the atmosphere (Panofsky and Dutton, 1984) buy may underestimate experimental results (Armitt and Counihan, 1968). A no-slip boundary condition was modelled at the surface following the approach of previous studies (Baghapour and Sullivan, 2017;Colli et al., 2016b). Further study with a no-slip wall condition under different turbulence conditions could lead to further insights into the influence of turbulence intensity on precipitation gauge collection efficiency.

6.1.2 Collection efficiency based on wind speed and hydrometeor fall velocity

~~Hydrometeors exhibit a wide variety of habits, sizes, shapes, and densities, influencing their aerodynamics and, in turn, their ability to be captured by the gauge.~~ The numerical model results ~~present study, using a spherical drag model,~~ demonstrates that collection efficiencies are similar for different hydrometeor types with different sizes, densities, masses, and drag values (spherical drag model), but similar fall velocities. This enables the characterization of collection efficiency independent of hydrometeor ~~type, diameter, density and drag~~characteristics other than fall velocity, ~~which~~ allowings for the broad application of ~~the~~ transfer functions with wind speed and fall velocity dependence ~~in the present study~~ to various hydrometeor types.

The numerical model results~~, which~~ captures ~~the~~ three-dimensional airflow and hydrometeor kinematics and illustrate the ~~(assuming a spherical drag model), exhibits a nonlinear~~ reductions in collection efficiency with increasing wind speed and decreasing hydrometeor fall velocity (Fig. 5). A slight nonlinearity in the collection efficiency relationship with wind speed is apparent, with the collection efficiency decreasing more rapidly at lower wind speeds and more gradually at higher wind speeds. This wind speed dependence has been demonstrated in previous studies (Nešpor and Sevruk, 1999;Thériault et al., 2012;Colli et al., 2016a;Baghapour et al., 2017), and is generally attributed to the three-dimensional velocity profile around the gauge influencing the trajectories and catchment of incoming hydrometeors.

~~The present study demonstrates~~ ~~A~~a strong nonlinear dependence on the hydrometeor fall velocity~~, as well~~ is apparent in Figs. 5 and 6. Hydrometeors with fall velocities above 5 m/s exhibit collection efficiencies close to 1, while lower hydrometeor fall velocities influence the rate of decrease of collection efficiency with wind speed ~~(Figs. 65 and 76)~~. Collection efficiency decreases are most pronounced below 2.0 m/s hydrometeor fall velocity, where a wide range of collection efficiencies are possible. This demonstrates the challenge in adjusting liquid, solid, and mixed precipitation accumulations in situations where different hydrometeor types and sizes – and with very different fall velocities – can occur. These findings support the conclusions of Thériault et al. (2012), who demonstrated large collection efficiency differences across dry snow and wet snow hydrometeors with different terminal velocities. The present findings also support those of Nešpor and Sevruk (1999), who showed that the wind-induced error increases rapidly for smaller raindrop sizes with lower terminal velocities.

Across rain, ice pellets, wet snow, and dry snow, the numerical collection efficiency results are very similar for hydrometeors with the same fall velocity over a wide range of wind speeds, despite differences in characteristics (size, density, and mass), as shown in Fig. 5. ~~Rain and ice pellets, with identical fall velocities, show very good agreement in collection efficiency results over all wind speeds. Collection efficiencies for rain and wet snow display good agreement up to approximately 4 m s^{-1} wind speed, above which collection efficiencies for rain are slightly higher than those for wet snow. This may be due to the higher~~

~~density of the rain hydrometeors relative to the wet snow hydrometeors, with hydrometeor inertia playing a role at higher wind speeds.~~Elevated collection efficiencies for rain compared with wet snow above 4 m s^{-1} wind speed may be due to the higher density of rain relative to wet snow, with hydrometeor inertia playing a role at higher wind speeds. ~~At 1.0 m s^{-1} fall velocity, dry snow and wet snow hydrometeors display similar collection efficiencies up to 3 m s^{-1} wind speed. Above this wind speed, the collection efficiency for dry snow decreases more rapidly than that for wet snow and rain. Conversely, rain and dry snow hydrometeors with lower fall velocities (0.5 and 0.75 m s^{-1}) have similar collection efficiencies for all wind speeds.~~

~~Collection efficiency differences between 1.0 m s^{-1} fall velocity dry snow and wet snow hydrometeors for wind speeds above 3 m s^{-1} may also be related to hydrometeor inertia, as the density of wet snow is approximately 150 times greater than that for dry snow at this fall velocity, as shown in Table 2. A similar rapid decrease in collection efficiency for dry snow has been demonstrated by Colli (2016b), with the collection efficiency decreasing to 0.35 at 3 m s^{-1} wind speed. This decrease may be due to the limitations of the spherical hydrometeor model; further investigation is recommended as an area for future work.~~

For dry snow with 1.0 m s^{-1} fall velocity, the collection efficiency decreases more rapidly relative to that for wet snow and rain hydrometeors with identical fall velocities above 3 m s^{-1} wind speed. A similar rapid decrease in collection efficiency for dry snow has been demonstrated by Colli (2016b). This decrease may be due to the limitations of the spherical hydrometeor model, which can overestimate hydrometeor volumes and buoyancies, particularly for non-spherical hydrometeors. Further investigation with non-spherical drag models is recommended as an area for future work.

~~Hydrometeors exhibit a wide variety of habits, sizes, shapes, and densities, influencing their aerodynamics and, in turn, their ability to be captured by the gauge. The present study, using a spherical drag model, demonstrates that collection efficiencies are similar for different hydrometeor types with different sizes, densities, masses, and drag values, but similar fall velocities. This enables the characterization of collection efficiency independent of hydrometeor type, diameter, density and drag, which allows for the broad application of the transfer function in the present study to various hydrometeor types. Assessment using non-spherical drag models is an area for future work.~~

6.1.3 ~~Empirical collection efficiency expression~~CFD transfer function

The ~~empirical expression~~CFD transfer function presented in Eq. 18 ~~(with a single set of~~ coefficients in ~~(~~Table 5) is based on the computational fluid dynamics results for an unshielded Geonor T-200B3 600 mm capacity precipitation gauge for wind speeds up to 10 m s^{-1}. This ~~expression~~transfer function provides a straightforward means of estimating the collection efficiency based on the wind speed and hydrometeor fall velocity. In operational monitoring networks, the hydrometeor fall velocity can be provided by disdrometers (Loffler-Mang and Joss, 2000;Sheppard and Joe, 2000;Bloemink and Lanzinger, 2005;Nitu et al., 2018), vertically pointing Doppler radars (Biral, 2019), or multi-frequency radar techniques (Kneifel et al., 2015). Assessment of these techniques for the measurement of hydrometeor fall velocity is an area for future work.

The ~~empirical expression~~CFD transfer function captures well the nonlinear change in collection efficiency with wind speed and hydrometeor fall velocity ~~that is~~ observed in the numerical model results across rain, ice pellet, wet snow, and dry snow hydrometeor types (Fig. ~~6~~5). This expression was derived from simulation results up to 10 m s^{-1} wind speed and should be

Formatted: Superscript

used with caution at higher wind speeds. Further, this transfer function has not been assessed experimentally for snow above 6 m s^{-1} in based on the present study for the CARE dataset results. The adjustment ofAdjusted precipitation accumulation estimates in this regime, where fall velocities are low and wind speeds are high, can be highly uncertain and should be treated with caution (Smith et al., 2020). Assessment of the transfer function at other sites under thesesuch conditions is an area for future work. Application to other gauge or shield combinations should also be investigated, as the flow dynamics around the gauge orifice are dependent on the specific gauge and shield geometry.

The fall velocity cutoff, shown in Fig. 76, corresponds to the fall velocity below which no hydrometeors are captured by the gauge for a given wind speed. In this case, the hydrometeors are unable to pass through the updraft region and local airflow around the gauge orifice to be captured by the gauge. As the wind speed increases, the fall velocity cutoff increases, asand it becomes more difficult for hydrometeors to overcome the updraft velocity and local airflow and be captured. This has important consequences for the overallintegral gauge collection efficiency, as hydrometeors below the fall velocity cutoff in the drop size distribution do not contribute to the total catchment. Previous studies have shown similar results with collection efficiencies decreasing to zero below a given hydrometeor size for liquid (Nešpor and Sevruk, 1999) and solid hydrometeor types (Thériault et al., 2012;Colli et al., 2016).

This finding agrees with the results of Nešpor and Sevruk (1999), who estimated the drop diameter below which the collection efficiency is zero for rain. The present formulation based on the fall velocity can be applied more broadly across rain and snow types for the unshielded Geonor gauge configuration. These results are based on time-averaged simulations, which provide an estimate of the mean velocities through the domain and have been shown to provide good overall agreement with experimental results (Baghapour et al., 2017). Further study using LES models, which can better resolve the eddy dynamics and temporal variations in the flow, and under different boundary conditions and turbulence scales representing different site conditions is recommended to better understand the collection efficiency under conditions with high wind speeds and low hydrometeor fall velocities.

6.1.4 Integral collection efficiency results

6.1.4.1 Wind speed dependence

The integral collection efficiency decreases nonlinearly with wind speed depending on the hydrometeor type and fall velocity. Large differences in the integral collection efficiency dependence with wind speed are apparent across different hydrometeor types and intensities. Previous studies have shown similar differences across liquid (Nešpor and Sevruk, 1999;Jarraud, 2008) and solid hydrometeor types (Colli et al., 2016b;Colli et al., 2020;Thériault et al., 2012). The fall velocities of snowflakes are generally smaller than those of raindrops; accordingly, the collection efficiency for snowfall at a given wind speed is lower than that for rainfall (Fig. 8). Similarly, dendrites have lower fall velocities than rimed dendrites and columns and plates, and lower collection efficiency.

The integral collection efficiency results decrease continuously with increasing wind speed as the magnitude of the updraft at the leading edge of the gauge increases, free-stream hydrometeor trajectories decrease, and hydrometeors trajectories become more closely coupled with the local airflow around the gauge. For dendrites, the nonlinearity in the integral collection efficiency is more pronounced, as collection efficiencies decrease to small but finite values at higher wind speeds. This is due to the smaller number of hydrometeors with sufficient fall velocity to be captured by the gauge at higher wind speeds.

The differences in collection efficiency for different precipitation characteristics (type, habit, precipitation intensity) illustrate the large variability that can be expected when the characteristics or fall velocity are not considered. This variability presents a particular challenge for mixed precipitation conditions, in which the precipitation type may not be well defined and can change rapidly over time. Both the wind speed and hydrometeor characteristics play important roles in determining collection efficiency. The proposed expression for the collection efficiency as a function of the wind speed and hydrometeor fall velocity (Eq. 18) provides a means of estimating the collection efficiency over different hydrometeor types and intensities, even if the precipitation type is not well defined.

~~The fall velocities of snowflakes are smaller than those of raindrops; accordingly, the collection efficiency for snowfall at a given wind speed is lower than that for rainfall (Fig. 9). Similarly, dendrites have lower fall velocities than rimed dendrites and columns and plates, and lower collection efficiency. This results in a lower collection efficiency for dendrites relative to the other crystal types. For a precipitation intensity of 0.5 mm h^{-1}, the overallintegral collection efficiency for dendrites remains very small above 7 m s^{-1} wind speed, as only a small number of hydrometeors have sufficient fall velocity to be captured by the gauge.~~

~~The overallintegral collection efficiency increases for higher precipitation intensities, due to the increased numbers of larger equivalent diameter crystals with higher fall velocities. This results from changes in the exponential factor in the hydrometeor size distribution with precipitation intensity, as shown by Gunn and Marshall (1957). Their work was based on ground-level filter paper measurements of equivalent hydrometeor diameters, representing the hydrometeor mass, instead of snowflake geometry. The hydrometeor size distribution of Gunn and Marshall has a lower offset and more rapid decay than that presented by Thériault et al. (2012), which is based on the measured snowflake diameter. Integrating the Gunn and Marshall drop size distribution, equivalent hydrometeor diameter, and fall velocity over the entire range of equivalent hydrometeor diameters gives a mutually consistent estimate for the precipitation intensity, supporting its use. Differences in collection efficiency with solid precipitation intensity are not well understood, and are difficult to distinguish from gauge uncertainties due to environmental conditions (e.g. wind, temperature). Regardless, these results demonstrate the variability in collection efficiency associated with the measurement of solid precipitation, even for hydrometeors of the same crystal habit.~~

~~The difference in collection efficiency for different precipitation characteristics illustrates the large variability that can be expected when the characteristics (type, habit, precipitation intensity) or fall velocity are not considered. This variability presents a particular challenge for mixed precipitation conditions in which the precipitation type may not be well defined and can change rapidly over time. Both the wind speed and hydrometeor characteristics play important roles in determining collection efficiency. The proposed expression for the collection efficiency as a function of the wind speed and hydrometeor~~

~~fall velocity (Eq. 18) provides a means of estimating the collection efficiency over different hydrometeor types and intensities, even if the precipitation type is not well defined.~~

The integral collection efficiency results using the CFD transfer function developed in the present study show good overall agreement with the results of Colli et al. (2016b) for wet snow and dry snow, as shown in Fig. 8. Integral collection efficiency values in the present study are slightly higher than those of Colli et al. (2016b), who demonstrated that their model results for dry snow slightly underpredict experimental results for temperatures below -4 °C. Differences between the two models may be due to differences in the gauge geometry and hydrometeor drag model, among other factors. The gauge geometry in the present study includes a refined orifice wall thickness and full-length orifice extending down into the gauge housing (Fig. 1). The peak velocities above the gauge in the present study are similar to those observed by Baghapour et al. (2017), who also used a refined orifice wall thickness and observed reduced peak velocities compared to the results of Colli et al. (2016b) as discussed in Sect. 6.1. Increases in the velocity magnitude over the gauge would be expected to decrease the collection efficiency in a manner similar to that for increased wind speed; hence, the higher peak velocities above the gauge in the results of Colli et al. (2016b) provide one explanation for the lower collection efficiency values observed.

Differences in the hydrometeor drag model may also contribute to differences in results among the two studies. The present study uses a spherical drag model similar to that used by Baghapour and Sullivan (2017), in which the drag coefficient varies based on the relative hydrometeor-to-air velocity over the path of the hydrometeor. The results of Colli et al. (2016b) are based on a constant drag model with a fixed drag coefficient over the hydrometeor path, following the approach of Thériault et al. (2012). Both Colli et al. (2015) and Baghapour and Sullivan (2017) showed that the constant drag model can overestimate the hydrometeor drag relative to empirical models, thereby reducing the collection efficiency.

The injection of hydrometeors from a horizontal plane in the present study ensures identical horizontal particle densities for each wind speed simulation following the approach of Nešpor and Sevruk (1999) for rain and Baghapour and Sullivan (2017) for snow. Injecting hydrometeors from a vertical plane, as done in previous studies (~~Thériault et al., 2012;~~Colli et al., 2016b), could lead to reduced horizontal particle densities and less certainty in numerical collection efficiency estimates for high wind speeds if the injection densities are not sufficiently high.

The present study defines the integral collection efficiency based on the ratio of precipitation rate or mass flux of precipitation captured by the gauge to that falling in air, following the approach of Nešpor and Sevruk (1999). This provides a consistent formulation for collection efficiency across rainfall and snowfall types. The collection efficiency defined by Colli et al. (2016b) for wet snow and dry snow is based on a 'volumetric' approach, with the fall velocity term in the integrand omitted. Omitting the fall velocity neglects the contribution of the rate of fall of hydrometeors to the overall precipitation rate, with higher fall velocities providing a greater precipitation rate. For the dry snow and wet snow comparison shown in Fig. 8 the differences between these two approaches are small.

The use of a continuous collection efficiency expression with wind speed and fall velocity dependence enables the derivation of integral collection efficiencies over intermediate sizes and fall velocities in the hydrometeor size distribution. Collection efficiencies can be computed at intermediate wind speed values using this approach as well, providing the smooth integral

collection efficiency curves shown in Fig. 8. Nešpor and Sevruk (1999) used a similar empirical approach for rain by developing an expression for the partial wind-induced error based on free-stream velocity and drop diameter applicable to Mk2, Hellman and ASTA gauges. The integral collection efficiency results of Colli et al. (2016b) were derived directly from numerical CE results for dry snow and wet snow at discrete sizes and wind speeds.

6.1.4.2 Precipitation intensity dependence

Knowledge of the precipitation type, intensity, and wind speed can provide a means for adjusting gauge catchment totals. For rainfall, the precipitation intensity has been shown to be an important parameter for the estimation of ~~overall~~integral collection efficiency (Nešpor and Sevruk, 1999;Jarraud, 2008). ~~OverallIntegral collection efficiencies for rainfall are generally close to 1 based on the results of Sect. 3.4.3 and shown in Fig. 10.~~ A gradual increase in ~~overall~~integral collection efficiency with precipitation intensity is observed for intensity values above 1 mm h^{-1}. Below this intensity, the ~~overall~~integral collection efficiency decreases more rapidly, with the rate of decrease depending on the rainfall type and wind speed. This is in general agreement with the results of Nešpor and Sevruk as presented in Jarraud (2008), who showed a sharper increase in the conversion factor (inverse of ~~overall~~integral collection efficiency) below 1 mm h^{-1}.

~~Overall~~Integral collection efficiencies for snowfall also increase with precipitation intensity, as higher intensities correspond with larger numbers of hydrometeors with higher fall velocities and increased collection efficiencies, as shown by Colli et al. (2020). ~~Overall~~Integral collection efficiencies for snowfall can be much lower than for rain, depending on the wind speed. Differences are apparent across different snowfall crystal habits (e.g. dendrites vs. dendrites and aggregates of plates), with the magnitude of differences increasing with wind speed. This illustrates the difficulty of adjusting snowfall measurements if the crystal habit is not known. The range of possible ~~overall~~integral collection efficiency values is even larger under conditions when solid, liquid, ~~or~~ and mixed precipitation can all be present. An additional challenge is presented by the measurement of low precipitation intensities for snowfall, where accumulations can be small relative to gauge uncertainties due to environmental factors (e.g. wind, temperature).

6.1.4.3 Hydrometeor fall velocity dependence

Integral collection efficiency differences across precipitation types are much smaller when stratified by wind speed and hydrometeor fall velocity (Fig. 10) than when stratified by wind speed and precipitation intensity (Fig. 9) or by wind speed alone (Fig. 7). This results from the ability of the hydrometeor fall velocity to capture differences in the integral collection efficiency across different hydrometeor types and precipitation intensities. The small differences in collection efficiency across different hydrometeor types with the same fall velocity are attributed to the nonlinearity in the relationship between collection efficiency and fall velocity over the mass-weighted distribution of hydrometeor fall velocities. ~~At a given wind speed, the relationship between the overallintegral collection efficiency and hydrometeor fall velocity shown in Fig. 11 exhibits more uniform profiles for different hydrometeor types and size distributions than the relationship between overallintegral collection efficiency and precipitation intensity shown in Fig. 10. The hydrometeor type and size distribution influence the mass-weighted~~

distribution of fall velocities, which, in turn, influence the ability of hydrometeors to be captured by the gauge at a given wind speed. The results in Fig. 1110 follow the general nonlinear profile of the empirical expressionCFD transfer function (Eq. 18, Fig. 76), with the hydrometeor fall velocity defining the overallintegral collection efficiency magnitude for a given wind speed. Thunderstorm rain with hydrometeor fall velocities above 3.5 m s^{-1} exhibits the highest overallintegral collection efficiencies, with values close to 1, followed by orographic rain, and then the different snowfall types with lower fall velocities decreasing towards 0. Dendrites, which have the lowest fall velocities, exhibit the lowest overallintegral collection efficiencies. Rimed dendrites have higher hydrometeor fall velocities relative to dendrites, and correspondingly higher overallintegral collection efficiencies. Dendrites and aggregates of plates exhibit a large range of fall velocities that depends on the size distribution, giving rise to a large range in collection efficiencies.

The small differences in collection efficiency across different hydrometeor types with the same fall velocity are attributed to the nonlinearity in the relationship between collection efficiency and fall velocity over the mass-weighted distribution of hydrometeor fall velocities. OverallIntegral collection efficiency differences across precipitation types are much smaller when stratified by wind speed and hydrometeor fall velocity (Fig. 11) than when stratified by wind speed and precipitation intensity (Fig. 10) or by wind speed alone (Fig. 9). This results from the ability of the hydrometeor fall velocity to capture differences in the overallintegral collection efficiency across different hydrometeor types and precipitation intensities.

Measurements of fall velocity can be obtained using a number of methods (Sect. 46.1.2), and are increasingly available through the deployment of disdrometers in operational networks. These measurements provide an independent assessment of the hydrometeor fall velocity, and together with gauge height wind speed estimates, can enable the adjustment of gauge precipitation accumulation measurements using Eq. (18). Adjustments using this approach can be applied over a range of hydrometeor types and even when the hydrometeor type may be unknown or uncertain.

46.2 Experimental Ddiscussion

Transfer functions were derived using accumulated precipitation amounts reported by automatic weighing precipitation gauges over 30 minute periods. A 0.25 mm accumulation threshold was applied to reference measurements from a DFAR, corresponding to an average precipitation rate of 0.5 mm/h over 30 minutes. A lower threshold of 0.075 mm was applied to measurements from the unshielded Geonor gauge to ensure collection efficiency estimates were reliable. This approach is consistent with that used in SPICE (Nitu et al., 2018) and the related derivation of transfer functions (Kochendorfer et al., 2017a). While automatic precipitation gauges can report at a temporal resolution of one minute, or even higher, the extension of the transfer function derivation and evaluation to other temporal periods, or different accumulation thresholds, is beyond the scope of this work.

The Kochendorfer et al. (2017a) universal transfer function with wind speed and air temperature dependence, $K_{Universal}$, was derived from measurements at eight SPICE sites in the interest of making the transfer function broadly applicable across different climates. This broad applicability is furthered by the widespread availability of air temperature and wind speed

measurements at meteorological stations. Recent studies have demonstrated that the performance of $K_{Universal}$ can vary substantially by site (Smith et al., 2020). Therefore, ~~site~~climate-specific K_{CARE} transfer function coefficients were also derived for comparison in the present study.

The K_{CARE} transfer function has a lower temperature threshold and exhibits larger increases in collection efficiency with increasing temperature relative to $K_{Universal}$ (Fig. ~~4a~~13a). These differences improved the overall RMSE for K_{CARE} by reducing the over-adjustment of some rain and mixed precipitation events; however, this improvement came at the expense of under-adjusting some snow events at warmer temperatures. The use of this approach warrants further study over longer periods to better understand the performance impacts of seasonal variability and assessment at other sites and climate regions with different precipitation characteristics and proportions.

Both the $K_{Universal}$ and K_{CARE} transfer functions performed well for snow, but were limited by their ability to distinguish among snow, rain, and mixed precipitation at temperatures between -5 °C and 2 °C. The largest uncertainties in collection efficiency and adjusted accumulation estimates were observed over this temperature range. Adjustments using wind speed and hydrometeor fall velocity, however, addressed this shortcoming and provided improved collection efficiency and adjusted accumulation estimates. ~~—~~The CFD transfer function, derived from time-averaged numerical simulation results over a wide range of wind speeds and hydrometeor fall velocities, resulted in low RMSE values overall and across rain, snow, mixed, and undefined precipitation types. These results ~~demonstrate~~ reinforce the fundamental importance of both wind speed and hydrometeor fall velocity on gauge collection efficiency ~~predicted~~ demonstrated by the CFD model results ~~of Part I~~ and results from earlier studies (Nešpor and Sevruk, 1999;Thériault et al., 2012).

The CFD~~is~~ transfer function exhibited the lowest RMSE of all transfer functions for mixed precipitation and for intermediate fall velocities between 1.5 m s^{-1} to 2.5 m s^{-1} (Table 9c), which is attributed to its nonlinear increase in collection efficiency with fall velocity. As this transfer function was derived theoretically, it is applicable across different sites and climate regimes with different types and relative proportions of hydrometeors. The present results also support the methodology for the CFD model, which can be extended to other shield and gauge combinations. For larger shields, it may be important to employ a more realistic vertical wind profile, with a zero-slip boundary condition at the earth's surface.

The HE1 transfer function showed good results for snow, supporting its use for the unshielded gauge. This approach is straightforward to implement based on its simplicity, and is less reliant on the accuracy of fall velocity estimates beyond the fall velocity ~~cut-off~~threshold. The collection efficiency for the HE1 transfer function decreases to ~~zero~~ 0.2 at a wind speed of ~~7.19~~5.75 m s^{-1}. This demonstrates the ~~limitation~~ challenge of adjusting unshielded gauge snow measurements at windy sites, where ~~the 30-minute mean wind speeds exceed the cutoff threshold value and~~ the captured accumulations ~~are~~ may be small relative to gauge uncertainties. The ~~e latter~~is can lead to large uncertainty in adjusted measurements, as demonstrated by other studies applying transfer functions to unshielded gauge measurements at windy sites (Smith et al., 2020). The ~~numerical~~ CFD transfer function results ~~in Part I~~ suggest a ~~more~~ gradual decrease in collection efficiency at higher wind speeds compared with the HE1 transfer function, as some hydrometeors with higher fall velocities are still able to be captured by the gauge; however, these accumulations remain small relative to gauge uncertainties, particularly in windy conditions, making them difficult to

assess experimentally. Further testing at other sites is recommended to better understand the collection efficiency for low fall velocity hydrometeors (light snow) under windy conditions above 6 m s^{-1}, which were not available in the CARE dataset. ~~The use of shielding or gauges with higher sensitivity could extend the applicability of this approach for use at windy sites.~~

A limitation of the HE1 transfer function is the minimal improvement in the RMSE for mixed precipitation and fall velocities between 1.5 m s^{-1} to 2.0 m s^{-1} relative to the K_{CARE} function. This is due to the over-adjustment of mixed precipitation events with fall velocities slightly below the cutoff value, and the under-adjustment of mixed precipitation events with fall velocities slightly above the cutoff. While the RMSE for mixed precipitation is still lower than that for adjustments based on temperature and wind speed ($K_{Universal}$, K_{CARE}), further improvements are obtained by using transfer functions with continuous fall velocity dependence; specifically, the CFD and HE2 transfer functions.

The HE2 transfer function, with a linear increase in collection efficiency with fall velocity, yields a greater reduction in the RMSE for mixed precipitation relative to the HE1 transfer function. The HE2 transfer function results show a higher RMSE for mixed precipitation than those for the CFD function, possibly due to the nonlinearity in the latter with fall velocity. The HE2 transfer function, however, yields the best RMSE results for snow, temperatures below -5 °C, and fall velocities below 1.5 m s^{-1}. Adjusted uncertainties for snow are approximately two times higher than those for rain, and show similar trends with increasing temperature and decreasing fall velocity. The former may be due to the lower event accumulations and greater adjustments for snow relative to rain, with measured values in closer proximity to the gauge uncertainty. The present approach of estimating the fall velocity using the POSS appears to perform well, overall;~~,~~ however, further study to better characterize the fall velocity distribution and changes over 30-minute time periods could lead to further improvements in the model under specific conditions such as mixed precipitation. While this transfer function was derived using the CARE dataset, it is more universally applicable than adjustments based on temperature, for which the relative proportions of rain, snow, and mixed precipitation at warmer temperatures can influence fit results. Further testing at other sites is recommended to assess this in different climate regions, with different hydrometeor types and associated fall velocities.

6.3 Application to operational networks

It is evident that the performance of catchment-type precipitation gauges is dependent on wind speed and the aerodynamic properties of both the gauge and incident hydrometeors (Nešpor and Sevruk, 1999;Thériault et al., 2012;Colli et al., 2016b). ~~Part I~~The modelling results of this study demonstrated this dependence from a theoretical perspective, resulting in a transfer function that incorporates hydrometeor fall velocity. The ~~present contribution~~experimental results validated this approach, which resulted in improved precipitation estimates from an unshielded gauge relative to those using surface temperature as a proxy for precipitation phase or type. Indeed, the use of surface temperature in this manner can be instructive (Kienzle, 2008;Harder and Pomeroy, 2013), but does not capture the conditions defining hydrometeor initiation and growth aloft (Stewart et al., 2015).

In this study, the fall velocity of hydrometeors reported by the POSS provided direct measurement of a key parameter related to the aerodynamics of the catchment process. In Canada, the POSS was deployed operationally to report present weather as

part of an automatic weather station. Globally, other types of disdrometers (e.g. OTT Parsivel^2, Thies Laser Precipitation Monitor) have been deployed operationally and can also provide hydrometeor vertical velocities. The uncertainty in fall velocity estimates for different technologies, hydrometeor types, sizes, fall velocities, wind speeds, and wind directions remains to be assessed. These sensors can also be useful for reporting present weather and verifying the occurrence of precipitation based on their high sensitivity (Nitu et al., 2018;Sheppard and Joe, 2000).

The results from this study demonstrate that the combined use of accumulation reports from an unshielded weighing gauge with fall velocities reported by a disdrometer, wind speed measurements, and an appropriate transfer function can greatly reduce the uncertainty of precipitation accumulation measurements. ~~At high wind speeds (> 7~~ 5.75 ~~m s^{-1}), the unshielded gauge catch may be insufficient for adjustment~~collection ~~efficiencies are difficult to assess due to the low measured quantities.~~ The extension of the approach in the present study to shielded precipitation gauges or gauge designs with higher sensitivity may provide a means of further reducing the measurement uncertainty for automatic gauges in windy environments. Application to light snow events and different event durations are other areas for future study.

~~5~~ 7 Conclusions

Hydrometeors exhibit a wide variety of habits, sizes, shapes, and densities, influencing their aerodynamics and, in turn, their ability to be captured by the gauge. Numerical modelling analysis for an unshielded Geonor T-200B3 600 mm precipitation gauge demonstrated that collection efficiencies are similar for different hydrometeor types with different sizes, densities, masses, and drag values, but similar fall velocities. The model results illustrated that wind speed influences the updraft magnitude and local airflow around the gauge orifice, while fall velocity affects the approach angle and degree of coupling between the hydrometeor trajectories and the local airflow. A novel CFD transfer function with wind speed and fall velocity dependence was developed from the model results. Two additional transfer functions with similar dependence were derived experimentally for unshielded Geonor T-200B3 precipitation gauges.

These t~~T~~hree collection efficiency transfer functions with gauge height wind speed and precipitation fall velocity dependence ~~are~~ were ~~presented~~ assessed experimentally ~~for unshielded Geonor T-200B3 precipitation gauges~~ and compared to universal and ~~site~~climate-specific transfer functions with wind speed and temperature dependence. These functions employ different models to adjust precipitation accumulation measurements for wind-induced undercatch, including:

(1) The nonlinear CFD transfer function model presented in ~~Part I~~Sect. 3, with collection efficiency decreasing nonlinearly with wind speed and increasing nonlinearly with precipitation fall velocity~~.~~;

(2) The HE1 transfer function, with a linear decrease in collection efficiency down to 0.2 with wind speed for 30-minute mean fall velocity below 1.93 m s^{-1}, and a collection efficiency of 1 above this fall velocity value~~.~~;

(3) The HE2 transfer function, with the linear wind speed dependence down to 0.2 collection efficiency, transitioning with increasing mode fall velocity to provide a collection efficiency of 1 when the mode fall velocity reaches 2.81 m s^{-1}.

These transfer functions were assessed using accumulation measurements from an unshielded precipitation gauge and DFAR gauge over 30-minute precipitation events during two winter seasons at the CARE test site in Egbert, ON, Canada. Estimates of fall velocity were provided by the POSS upward-facing Doppler radar.

All The transfer functions presented in this studywith mean wind speed and fall velocity dependence improved the agreement between the 30-minute adjusted precipitation accumulation values and DFAR reference values relative to the $K_{Universal}$ and K_{CARE} transfer functions based onwith mean wind speed and air temperature dependence. The CFD transfer function agreed well with experimental results over all observed fall velocities, supporting the use of the numerical modelling approach in Part I and providinged the lowest RMSE for mixed precipitation. The HE1 transfer function captured the collection efficiency trends for rain and snow well, with the collection efficiency for rain close to 1 and the collection efficiency for snow decreasing with wind speed. The HE2 transfer function better captured the collection efficiency for mixed precipitation with fall velocities between 1.2 m s^{-1} to 4.6 m s^{-1}. SiteClimate specific transfer functions (K_{CARE}) based on wind speed and temperature can also be employed to reduce the RMSE of measurements from unshielded weighing gauges relative to universal functions. The most significant reductions in RMSE, however, were observed for the transfer functions based on wind speed and hydrometeor fall velocity.

The results of this study further demonstratereinforce the important role of fall velocity on collection efficiency shown in previous studies (Nešpor and Sevruk, 1999;Thériault et al., 2012). Adjustment approaches incorporating fall velocity show tremendous value and potential, particularly in the general situation where DFAR measurements are not feasible, and can be applied where the precipitation type is complex (e.g. snow transitioning to rain), uncertain, or even unknown. These approaches warrant further investigation at different sites with different precipitation characteristics, fall velocities, and wind speeds. Further study to assess the collection efficiency relationships with wind speed and precipitation fall velocity for different shield configurations, as well as assessing the fall velocity using other means, including disdrometers or remote sensing, is also recommended.

Disclaimer. Many of the results presented in this work were obtained as part of the Solid Precipitation Intercomparison Experiment (SPICE) conducted on behalf of the World Meteorological Organization (WMO) Commission for Instruments and Methods of Observation (CIMO). The POSS was not included as part of the SPICE intercomparison. The analysis and views described herein are those of the authors, and do not represent the official outcome of WMO-SPICE. Mention of commercial companies or products is solely for the purposes of information and assessment within the scope of the present work, and does not constitute a commercial endorsement of any instrument or instrument manufacturer by the authors or the WMO.

Author contribution. J.H. was the lead author and was responsible for the CFD analysis, methodology, analysis, visualization, and manuscript preparation and editing. M.E.E. provided guidance for the methodology, analysis, visualization, and writing – review and editing. P.I.J. provided guidance for the analysis, interpretation of results, visualization, and writing – review and editing. P.E.S. provided guidance for the analysis, interpretation of results, and writing – review and editing.

Acknowledgements. The authors would like to acknowledge the encouragement and support of Rodica Nitu for this field of study. Thank-you to Christine Best, Pierrette Blanchard, and Sorin Pinzariu for supporting this work and Brian Sheppard for helpful discussions regarding the POSS. Thank-you to Hagop Mouradian, Sorin Pinzariu, and Lillian Yao for the data logger programming, electrical wiring, site maintenance, data ingest, and quality control for the CARE test site. The authors would also like to thank the WMO-SPICE team for their contributions and for discussions inspiring many facets of this work. We also thank John Kochendorfer and the anonymous reviewers for providing thoughtful reviews of the original version of this manuscript, and greatly improving the quality of this paper.

Data availability. The unshielded and reference event accumulations, wind speed, temperature, mean and mode fall velocity, and precipitation type data used in this study will be made available in a suitable online repository. The flow simulation and collection efficiency results from this study shown in Figs. 3, 5, 7, 8, 9, and 10 will be made available in a suitable online repository.

Competing interests. The authors declare that they have no conflict of interest.

References

Armitt, J., and Counihan, J.: The simulation of the atmospheric boundary layer in a wind tunnel, Atmospheric Environment, 2, 49-71, https://doi.org/10.1016/0004-6981(68)90019-x, 1968.

Atlas, D.: Optical extinction by rainfall, Journal of Meteorology, 10, 486-488, https://doi.org/10.1175/1520-0469(1953)010<0486:OEBR>2.0.CO;2, 1953.

Baghapour, B., and Sullivan, P. E.: A CFD study of the influence of turbulence on undercatch of precipitation gauges, Atmospheric Research, 197, 265-276, https://doi.org/10.1016/j.atmosres.2017.07.008, 2017.

Baghapour, B., Wei, C., and Sullivan, P. E.: Numerical simulation of wind-induced turbulence over precipitation gauges, Atmospheric Research, 189, 82-98, https://doi.org/10.1016/j.atmosres.2017.01.016, 2017.

Beard, K. V.: Terminal velocity and shape of cloud and precipitation drops aloft, J. Atmos. Sci., 33, 851-864, https://doi.org/10.1175/1520-0469(1976)033<0851:TVASOC>2.0.CO;2, 1976.

Biral micro rain radar: https://www.biral.com/product/micro-rain-radar/, access: June 25, 2019, 2019.

Blanchard, D. C.: Raindrop size distribution in Hawaiian rains, J. Meteor., 10, 457-473, https://doi.org/10.1175/1520-0469(1953)010<0457:RSDIHR>2.0.CO;2, 1953.

Bloemink, H. J. I., and Lanzinger, E.: Precipitation type from Thies disdrometers, Bucharest, Romania, 4-7, 2005.

Canada: Precipitation Occurrence Sensor System (POSS) Technical Manual, Environment Canada, 1995.

Chubb, T., Manton, M. J., Siems, S. T., Peace, A. D., and Bilish, S. P.: Estimation of wind-induced losses from a precipitation gauge network in the Australian Snowy Mountains, Journal of Hydrometeorology, 16, 2619-2638, https://10.1175/JHM-D-14-0216.1, 2015.

Colli, M.: Assessing the accuracy of precipitation gauges: a CFD approach to model wind induced errors, PhD, Department of Civil, Chemical and Environmental Engineering, University of Genova, 2014.

Colli, M., Lanza, L. G., Rasmussen, R., and Thériault, J. M.: A CFD Evaluation of wind induced errors in solid precipitation measurements, TECO 2014, St. Petersburg, Russia, 2014.

Colli, M., Rasmussen, R., Thériault, J. M., L.G., L., Baker, B., and Kochendorfer, J.: An improved trajectory model to evaluate the collection performance of snow gauges, J. App. Met. & Clim., 54, 1826-1836, https://doi.org/10.1175/JAMC-D-15-0035.1, 2015.

Colli, M., Lanza, L. G., Rasmussen, R., and Thériault, J. M.: The collection efficiency of shielded and unshielded precipitation gauges. Part I: CFD airflow modeling, J. Hydromet., 17, 231-243, https://doi.org/10.1175/JHM-D-15-0010.1, 2016a.

Colli, M., Lanza, L. G., Rasmussen, R., and Thériault, J. M.: The collection efficiency of shielded and unshielded precipitation gauges. Part II: Modeling particle trajectories., J. Hydromet., 17, 245-255, https://doi.org/10.1175/JHM-D-15-0011.1, 2016b.

Colli, M., Stagnaro, M., Lanza, L. G., Rasmussen, R., and Thériault, J. M.: Adjustments for Wind-Induced Undercatch in Snowfall Measurements Based on Precipitation Intensity, Journal of Hydrometeorology, 21, 1039-1050, https://doi.org/10.1175/JHM-D-19-0222.1, 2020.

Constantinescu, G. S., Krajewski, W. F., Ozdemir, C. E., and Tokyay, T.: Simulation of airflow around rain gauges: comparison of LES and RANS models, Adv. Water Resour., 30, 43-58, https://doi.org/10.1016/j.advwatres.2006.02.011, 2007.

Goodison, B. E.: Accuracy of Canadian snow gauge measurements, Journal of Applied Meteorology, 17, 1542-1548, https://doi.org/10.1175/1520-0450(1978)017<1542:AOCSGM>2.0.CO;2, 1978.

Goodison, B. E., Louie, P. Y. T., and Yang, D.: WMO solid precipitation measurement intercomparisonWMO/TD 872, 1998.

Gunn, K. L. S., and Marshall, J. S.: The distribution with size of aggregate snowflakes, Journal of Meteorology, 15, 452-461, https://doi.org/10.1175/1520-0469(1958)015<0452:TDWSOA>2.0.CO;2, 1957.

Haider, A., and Levenspiel, O.: Drag coefficient and terminal velocity of spherical and nonsperical particles, Powder technology, 58, 63-70, https://doi.org/10.1016/0032-5910(89)80008-7, 1989.

Harder, P., and Pomeroy, J.: Estimating precipitation phase using a psychrometric energy balance method, Hydrological Processes, 1901-1914, 10.1002/hyp.9799, 2013.

Henderson, C. B.: Drag coefficients of spheres in continuum and rarefied flows, American Institute of Aeronautics & Astronautics Journal, 14, 707-708, https://doi.org/10.2514/3.61409, 1976.

Hoover, J., Sullivan, P. E., Joe, P. I., and Earle, M. E.: Unshielded precipitation gauge collection efficiency with wind speed and hydrometeor fall velocity. Part I: modelling results, Hydol. Earth Syst. Sci. Discuss., https://doi.org/10.5194/hess-2020-553, 2020.

Jarraud, M.: Guide to meteorological instruments and methods of observation, World Meteorological Organization, Geneva, Switzerland, 2008.

Kato, M., and Launder, B.: The modelling of turbulent flow around stationary and vibrating square cylinders, Ninth Symposium of Turbulent Shear Flows, Kyoto, Japan, 1993.

Khvorostyanov, V. I., and Curry, J. A.: Fall velocities of hydrometeors in the atmosphere: refinements to a continuous analytical power law, Journal of Atmospheric Sciences, 62, 4343-4357, https://doi.org/10.1175/JAS3622.1, 2005.

Kienzle, S. W.: A new temperature based method to separate rain and snow, Hydrological Processes, 5067-5085, 10.1002/hyp.7131, 2008.

Kneifel, S., Von Lerber, A., Tiira, J., Moisseev, D., Kol-lias, P., and Leinonen, J.: Observed relations between snowfall microphysics and triple-frequency radar measurements, J. Geophys. Res.-Atmos., 120, 6034-6055, https://doi.org/10.1002/2015JD023156, 2015.

Kochendorfer, J., Nitu, R., Wolff, M., Mekis, E., Rasmussen, R., Baker, B., Earle, M. E., Reverdin, A., Wong, K., Smith, C. D., Yang, D., Roulet, Y.-A., Buisan, S., Laine, T., Lee, G., Aceituno, J. L. C., Alastrue, J., Isaksen, K., Meyers, T., Brækkan, R., Landolt, S., Jachcik, A., and Poikonen, A.: Analysis of single-Alter-shielded and unshielded measurements of mixed and solid precipitation from WMO-SPICE, Hydrol. Earth Syst. Sci., 21, 3525-3542, https://doi.org/10.5194/hess-21-3525-2017, 2017a.

Kochendorfer, J., Rasmussen, R., Wolff, M., Baker, B., Hall, M. E., Meyers, T., Landolt, S., Jachcik, A., Isaksen, K., Braekkan, R., and Leeper, R.: The quantification and correction of wind-induced precipitation measurement errors, Hydrol. Earth Syst. Sci., 1793-1989, https://doi.org/10.5194/hess-21-1973-2017, 2017b.

Kochendorfer, J., Nitu, R., Wolff, M., Mekis, E., Rasmussen, R., Baker, B., M.E., E., Reverdin, A., Wong, K., Smith, C. D., Yang, D., Roulet, Y.-A., Meyers, T., Buisan, S., Isaksen, K., Braekkan, R., Landolt, S., and Jachcik, A.: Testing and development of transfer

functions for weighing precipitation gauges in WMO-SPICE, Hydol. Earth Syst. Sci., 22, 1437-1452, https://doi.org/10.5194/hess-22-1437-2018, 2018.

Koltzow, M., Casati, B., Haiden, T., and Valkonen, T.: Verification of solid precipitation forecasts from numerical weather prediction models in Norway, Weather and Forecasting, https:\\10.1175/WAF-D-20-0060.1., 2020.

Launder, B., and Spalding, D.: The numerical computation of turbulent flows, Computer methods in applied mechanics and engineering, 3, 269-289, https://doi.org/10.1016/B978-0-08-030937-8.50016-7, 1974.

Loffler-Mang, M., and Joss, J.: An optical distdrometer for measuring size and velocity of hydrometeors, JOAT, 130-139, https://doi.org/10.1175/1520-0426(2000)017<0130:AODFMS>2.0.CO;2, 2000.

Nešpor, V., and Sevruk, B.: Estimation of wind-induced error of rainfall gauge measurements using a numerical simulation, Journal of Atmospheric & Oceanic Technology, 16, 450-464, https://doi.org/10.1175/1520-0426(1999)016<0450:EOWIEO>2.0.CO;2, 1999.

Nitu, R., Roulet, Y.-A., Wolff, M., Earle, M., Reverdin, A., Smith, C., Kochendorfer, J., Morin, S., Rasmussen, R., Wong, K., Alastrué, J., Arnold, L., Baker, B., Buisán, S., Collado, J. L., Colli, M., Collins, B., Gaydos, A., Hannula, H.-R., Hoover, J., Joe, P., Kontu, A., Laine, T., Lanza, L., Lanzinger, E., Lee, G., Lejeune, Y., Leppänen, L., Mekis, E., Panel, J.-M., Poikonen, A., Ryu, S., Sabatini, F., Theriault, J., Yang, D., Genthon, C., Heuvel, F. v. d., Hirasawa, N., Konishi, H., Nishimura, K., and Senese, A.: WMO Solid Precipitation Intercomparison Experiment (SPICE), World Meteorological Organization131, 2018.

Panofsky, H. A., and Dutton, J. A.: Atmospheric turbulence: models and methods for engineering applications, Wiley-Interscience, 1984.

Ramana, M., Gupta, B. V., and Gupta, S. C.: Precipitation characteristics based on raindrop size measurements at Delhi and Khandala during southwest monsoon., J. Sci. Ind. Res., 18A, 352-371, 1959.

Rasmussen, R., Dixon, M., Hage, F., Cole, J., Wade, C., Tuttle, J., McGettigan, S., Carty, T., Stevenson, L., and Fellner, W.: Weather support to deicing decision making (WSDDM): a winter weather nowcasting system, Bulletin of the American Meteorological Society, 82, 579-595, 2001.

Rasmussen, R., Baker, B., Kochendorfer, J., Meyers, T., Landolt, S., Fischer, A. P., Black, J., Theriault, J. M., Kucera, P., Gochis, D., Smith, C., Nitu, R., Hall, M., Ikeda, K., and Gutmann, E.: How well are we measuring snow: the NOAA/FEE/NCAR winter precipitation test bed, BAMS, http://dx.doi.org/10.1175/BAMS-D-11-00052.1, 2012.

Rasmussen, R. M., Vivekanandan, J., Cole, J., Meyers, B., and Masters, C.: The estimation of snowfall rate using visibility, Journal of Applied Meteorology, 38, 1542-1563, https://doi.org/10.1175/1520-0450(1999)038<1542:TEOSRU>2.0.CO;2, 1999.

Sevruk, B. H., J.-A.; Tettamanti, R.: The effect of orifice rim thickness on the wind speed above precipitation gauges, Atmospheric Environment, 28, 1939-1944, https://doi.org/10.1016/1352-2310(94)90334-4, 1994.

Sheppard, B. E.: Measurement of raindrop size distributions using a small Doppler radar, J. Atmos. Oceanic Technol., 7, 255-268, https://doi.org/10.1175/1520-0426(1990)007<0255:MORSDU>2.0.CO;2, 1990.

Sheppard, B. E., and Joe, P. I.: Comparison of raindrop size distribution measurements by a Joss-Waldvogel disdrometer, a PMS 2DG spectrometer, and a POSS dopler radar, J. Atmos. Oceanic Technol., 11, 874-887, https://doi.org/10.1175/1520-0426(1994)011<0874:CORSDM>2.0.CO;2, 1994.

Sheppard, B. E., Joe, P., Oleskiw, M., and Kouwen, N.: Quantitative measurement of snow mass concentration using the POSS, Conf. on Observations and Instrumentation, Charlotte, NC, 1995.

Sheppard, B. E., and Joe, P. I.: Automated precipitation detection and typing in winter: a two-year study, J. Atmos. Oceanic Technol., 17, 1493-1507, https://doi.org/10.1175/1520-0426(2000)017<1493:APDATI>2.0.CO;2, 2000.

Sheppard, B. E.: Sampling errors in the measurement of rainfall parameters using the Precipitation Occurence Sensor System (POSS), J. Atmos. Oceanic Technol., 24, 125-140, https://doi.org/10.1175/JTECH1956.1, 2007.

Sheppard, B. E., and Joe, P. I.: Performance of the Precipitation Occurrence Sensor System as a Precipitation Gauge, Journal of Atmospheric & Oceanic Technology, 25, https://doi.org/10.1175/2007JTECHA957.1, 2008.

Smith, C. D.: Correcting the wind bias in snowfall measurements made with a Geonor T-200B precipitation gauge and alter wind shield, 87th Annual AMS Meeting, San Antonio, TX, 2007.

Smith, C. D., Ross, A., Kochendorfer, J., Earle, M. E., Wolff, M., Buisan, S., Roulet, Y.-A., and Laine, T.: Evaluation of the WMO Solid Precipitation Intercomparison Experiment (SPICE) transfer functions for adjusting the wind bias in solid precipitation measurements, Hydol. Earth Syst. Sci., 24, 4025-4043, https://doi.org/10.5194/hess-24-4025-2020, 2020.

SolidWorks: Enhanced turbulence modeling in SolidWorks flow simulation, USAMKTURBMODWPENG0313, 2013.

SolidWorks: SolidWorks Flow Simulation Technical Reference, 2019.

Spalding, D. B.: A single formula for the law of the wall, J. Appl. Mech., 28, 455-458, 1961.

Stewart, R. E., Thériault, J. M., and Henson, W.: On the characteristics of and processes producing winter precipitation types near 0C, Bull. Amer. Meteor. Soc., 96, 623-639, https://10.1175/BAMS-D-14-00032.1, 2015.

Thériault, J. M., Rasmussen, R., Ikeda, K., and Landolt, S.: Dependence of Snow Gauge Collection Efficiency on Snowflake Characteristics, Journal of Applied Meteorology & Climatology, 51, https://doi.org/10.1175/JAMC-D-11-0116.1, 2012.

Thériault, J. M., Rasmussen, R., Petro, E., Trépanier, J.-Y., Colli, M., and Lanza, L. G.: Impact of wind direction, wind speed, and particle characteristics on the collection efficiency of the double fence intercomparison reference, Journal of Applied Meteorology and Climatology, 54, 1918-1930, https://doi.org/10.1175/JAMC-D-15-0034.1, 2015.

Ulbrich, C. W.: Natural variations in the analytical form of the raindrop size distribution, Journal of Climate and Applied Meteorology, 22, 1764-1775, https://doi.org/10.1175/1520-0450(1983)022<1764:NVITAF>2.0.CO;2, 1983.

Wolff, M. A., Isaksen, K., Petersen-Øverleir, A., Ødemark, K., Reitan, T., and Brækkan, R.: Derivation of a new continuous adjustment function for correcting wind-induced loss of solid precipitation: results of a Norwegian field study, Hydrol. Earth Syst. Sci., 19, 951-967, https://doi.org/10.5194/hess-19-951-2015, 2015.

Yang, D., Goodison, B. E., Metcalfe, J. R., Golubev, V. S., Bates, R., Pangburn, T., and Hanson, C. L.: Accuracy of NWS 8" standard nonrecording precipitation gauge: results and application of WMO intercomparison, Journal of Atmospheric & Oceanic Technology, 15, 54-68, https://doi.org/10.1175/1520-0426(1998)015<0054:AONSNP>2.0.CO;2, 1998.

Yang, D., Kane, D., and Zhang, Z.: Bias corrections of long-term (1973-2004) daily precipitation data over the northern regions, Geophysical Research Letters, 32, 1-5, https://doi.org/10.1029/2005GL024057, 2005.

Yang, D., and Simonenko, A.: Comparison of Winter Precipitation Measurements by Six Tretyakov Gauges at the Valdai Experimental Site, Atmosphere-Ocean, 1-15, https://doi.org/10.1080/07055900.2013.865156, 2013.

Yang, D.: Double fence intercomparison reference (DFIR) vs. bush gauge for 'true' snowfall measurement, Journal of Hydrology, 509, 94-100, https://doi.org/10.1016/j.jhydrol.2013.08.052, 2014.